A S M SHANAWAZ UDDIN

VEGETATION AND PLATFORM GEOMETRY EFFECTS ON WAKE ATTENUATION IN WETLANDS

UNIVERSIDADE DO ALGARVE

Faculdade de Ciências e Tecnologia

2025

A S M SHANAWAZ UDDIN

VEGETATION AND PLATFORM GEOMETRY EFFECTS ON WAKE ATTENUATION IN WETLANDS

Master's in Coastal Hazards, Risks, Climate Change Impacts and Adaptation

Performed under the supervision of:
A. Rita Carrasco &
María E. Maza Fernández

UNIVERSIDADE DO ALGARVE

Faculdade de Ciências e Tecnologia

2025

Declaração de autoria de trabalho

Declaration of Authorship of work

VEGETATION AND PLATFORM GEOMETRY EFFECTS ON WAKE ATTENUATION IN WETLANDS

Declaro ser o autor deste trabalho, que é original e inédito. Autores e trabalhos consultados estão devidamente citados no texto e constam da listagem de referências incluída.

I declare to be the author of this work, which is original and unpublished. Authors and works consulted are duly cited in the text and are included in the list of references.

A S M Shanawaz Uddin
Faro, 14 July 2025

COPYRIGHT

ACKNOWLEDGEMENT

First and foremost, I would like to express my sincere gratitude to my dedicated thesis supervisors, Dr. A. Rita Carrasco and Dr. María E. Maza Fernández, for their invaluable guidance, encouragement, and support throughout this research. Their expertise and commitment have been crucial to the completion of this work. I am also deeply thankful for the continuous advice and thoughtful insights from Dr. Óscar Ferreira, whose mentorship has significantly enriched my academic journey.

I gratefully acknowledge the support of the Erasmus+ Programme of the European Union, which enabled me to pursue this prestigious Joint MSc degree. Special thanks go to the coordinators of the COASTHazar Programme, Dr. Alvaro Semedo, Prof. Javier López Lara, and Dr. Óscar Ferreira, for their exceptional leadership and dedication.

My heartfelt thanks also go to all the professors, instructors, mentors, and staff at Universidad de Cantabria, IHE Delft Institute for Water Education, and Universidade do Algarve. Your teaching, guidance, and support have played a vital role in both my personal and academic development.

To my COASTHazar classmates, thank you for the friendship, collaboration, and shared experiences. Your friendship has made this journey more meaningful and memorable.

A special note of appreciation goes to all my previous institutional teachers and colleagues, who have been my refuge during difficult times and my source of inspiration throughout this process.

Lastly, I dedicate this work to my beloved wife, Kamrun Nahar, whose unwavering support, love, and patience have sustained me every step of the way. Her encouragement has been the foundation upon which this achievement stands.

ABSTRACT

Wetlands play a vital role in coastal protection by dissipating wave energy, reducing flooding risks, stabilizing shorelines, and offering sustainable alternative to engineered defenses. Despite extensive research on wind wave attenuation by salt marsh vegetation, further studies are needed to quantify wetlands ability to mitigate the impact of wind and boat generated waves, and enhance their use as a Nature-based Solution towards sustainable coastal protection strategies. The aim of this study was to investigate the role of wetlands vegetation and morphology in dissipating wave energy in the Ria Formosa lagoon, southern Portugal. This was accomplished through a comprehensive analysis of how vegetation characteristics and profile morphology influence wave attenuation, utilizing field measurements and numerical modelling. Specifically, after understanding physical mechanisms and validate the SWAN model, this model was employed to assess the effects of different boat wake intensities, vegetation densities, and platform geometries on wave energy reduction. The results obtained demonstrate that wetland platforms with gentle slopes and around 100 meters length seemed to be the most effective on reducing wave energy, but they only contribute to 10% of the overall wave attenuation, with the remaining attenuation being promoted by the vegetation. Densely vegetated profile achieved 68% wave energy reduction compared to sparse or non-vegetated ones. *Zostera noltei* provided greater attenuation than *Spartina maritima* at only higher wave heights. Nevertheless, the occurrence of mixed-species vegetation proved to be more effective than just having single vegetation, for the same geometry. Wave attenuation increased with both wave height and vegetation density, up to a saturation point at around 4800 stems/m^2 for *Zostera noltei* and 1400 stems/m^2 for *Spartina maritima*. These findings suggest that optimizing both biological and platform characteristics is essential for maximizing coastal protection. The research highlights the need for comprehensive field measurements, with diverse ecological settings, tidal dynamics, varied geometries and salt marsh species to more effectively capture complex interactions between waves and wetland ecosystems. The outcomes provide practical recommendations for designing and managing resilient wetlands to support sustainable and adaptive coastal defense strategies.

Keywords: Wetlands; Boat wakes; Nature-based Solutions; Vegetation species; SWAN model; Profile morphology; Coastal protection.

RESUMO

As zonas húmidas desempenham um papel vital na proteção costeira, dissipando a energia das ondas, reduzindo os riscos de inundações, estabilizando as linhas de costa e oferecendo uma alternativa sustentável proteção pesada. Apesar da extensa investigação já existente sobre a atenuação de ondas geradas pelo vento pela vegetação de sapal, são necessários mais estudos científicos para quantificar a capacidade das zonas húmidas na atenuação do impacto das ondas geradas pelo vento e por barcos, e melhorar a sua utilização como uma Solução Baseada na Natureza, tendo em vista a adoção de estratégias sustentáveis de proteção costeira. Estudo teve como objetivo investigar o papel da vegetação hlófita e da morfologia das zonas húmidas na dissipação da energia de ondas geradas por barco na Ria Formosa, sul de Portugal. Para tal, realizou-se uma análise abrangente de como as características da vegetação e a morfologia do perfil influenciam a atenuação das ondas, utilizando medições de campo e modelação numérica. Após a compreensão dos mecanismos físicos envolvidos e validação do modelo, o modelo SWAN foi utilizado para avaliar os efeitos de diferentes densidades de vegetação e geometrias de planícies de maré e sapais na redução da energia das ondas. Os resultados obtidos demonstram que as morfologias de zonas húmidas com declives suaves e com maiores extensões (cerca de 100 metros de comprimento) parecem ser as mais eficazes na redução da energia das ondas, contribuindo apenas para 10% da atenuação global das ondas, sendo a restante atenuação promovida pela vegetação. O perfil mais densamente vegetado resultou em 68% de redução da energia das ondas, em comparação com os perfis com vegetação esparsa ou sem vegetação. A *Zostera noltei* proporcionou maior atenuação do que a *Spartina marítima*, mas apenas para alturas de onda mais elevadas. A ocorrência de vegetação de diferentes espécies, ao mesmo tempo, revelou-se mais eficaz do que apenas ter uma única tipologia de vegetação, para a mesma geometria. A atenuação das ondas aumentou com a altura das ondas e a densidade da vegetação, até um ponto de saturação de cerca de 4800 hastes/m^2 para *Zostera noltei* e 1400 hastes/m^2 para *Spartina maritima*. Estes resultados sugerem que a otimização das características biológicas e da morfologia das zonas húmidas é essencial para maximizar o potencial de proteção costeira. Deste trabalho destaca-se a necessidade de medições de campo abrangentes, considerando diversos cenários ecológicos, dinâmicas de marés, geometrias variadas e espécies de vegetação presentes

no sapal, para captar de forma mais eficaz as interações complexas entre ondas e ecossistemas de zonas húmidas. Os resultados fornecem recomendações práticas para a conceção e gestão de zonas húmidas resilientes, de forma a apoiar estratégias de defesa costeira sustentáveis e adaptativas.

Palavras-chave: Zonas húmidas; Ondas de barcos; Soluções baseadas na Natureza; Espécies de vegetação; Modelo SWAN; Morfologia de perfil; Proteção costeira.

TABLE OF CONTENTS

LIST OF FIGURES

LIST OF FIGURES (continued)

LIST OF TABLES

LIST OF EQUATIONS

LIST OF ACRONYMS

NbS	Nature-based Solutions
LM	Low Marsh
TF	Tidal Flat
RTK-DGNSS	Real-time kinematic Differential Global Navigation Satellite System
PTs	Pressure Transducers
MSL	Mean-Sea Level

LIST OF SYMBOLS

F_d	Drag force (N)
C_D	Drag coefficient
ρ	Density of the water (kg/m^3)
A_v	Vegetation frontal area per unit volume (m^2)
$\|u\|$	Flow velocity magnitude (m/s)
H_{rms}	Root mean square wave height (m)
$H_{rms\ in}$	Root mean square incident wave height (m)
H_s	Significant wave height (m)
T_{mean}	Mean wave period (second)
β	Wave damping coefficient (m^{-1})
d	Stem diameter (m)
N	Number of stems per square meter (stems/m^2)
h	Water depth (m)
k	Wave number (m^{-1})
h_v	Vegetation height (m)
L/h	Wavelength to depth ratio
H_s/h	Non-dimensional wave height
H_s/L	Wave steepness
N^*	Combined vegetation damping parameter
KC	Keulegan-Carpenter number
$U\ (z)$	Maximum horizontal orbital velocity (m/s)

I. Introduction

1.1. Motivation

Nature-based solution (NbS) is defined as actions to protect, sustainably manage, and restore natural and modified ecosystems that address societal challenges effectively and adaptively, simultaneously benefiting people and nature (IUCN, 2016). Coastal NbS is referred to as sustainable management and planning for coastal areas, which in turn enhances adaptability against coastal hazards and climate change threats. NbS are considered as long term coastal protection due to self-recovery rate after storms and low failure probability than man-made structures (Castagno et al., 2021).

Wetlands play an essential role as NbS in mitigating the effects of waves, functioning as natural buffer zones that offer protection to shorelines and reduce the impact of coastal flooding (Gedan et al., 2011). Their wave energy dissipation capabilities are crucial for safeguarding both human populations and property, yielding profound socioeconomic benefits. This wave attenuation capacity is of paramount importance in protecting coastal communities from waves impacts and rising sea levels (Möller et al., 2014; Shepard et al., 2011). By providing these ecosystem service, salt marshes shield millions of people globally, offering significant protection against flooding events. Other invaluable services extend beyond flood defense, such as shoreline stabilization, carbon sequestration, water purification, increasing biodiversity and encouraging human well-being (Mcleod et al., 2011; Reguero et al., 2020; Siverd et al., 2020; Thorslund et al., 2017). However, their ability to protect coastal areas from flooding has emerged as one of their most significant contributions, particularly in light of climate change-induced risks. These ecosystems offer a cost-effective and sustainable alternative to conventional engineering approaches by leveraging natural processes (van Zelst et al., 2021). In many cases, this natural defense mechanism has proven more effective and reliable than artificial structures, especially when combined with other NbS. For example, the use of salt marshes in conjunction with levees,

can lead to significant cost reductions and enhance the longevity of these defenses by lowering maintenance demands (van Zelst et al., 2021). So, there is a growing interest in utilizing NbS, like wetlands including salt marshes, as an effective alternative for flood risk mitigation.

Wave height decay is observed when propagating through vegetation meadow which is explained by wave decay co-efficient (Bradley and Houser, 2009). Spatially dense vegetation cover acts as a barrier to prevent wave actions (Paul and Amos, 2011). However, the effectiveness of vegetation to attenuate boat wake is still dearth of knowledge until now, despite numerous studies have quantified wind wave attenuation (Passaro et al., 2021). Wave attenuation is linked with water depth, wave characteristics, plant density, and vegetation type. The latter proved based on mathematical or physical modelling by Magdalena et al. (2022). Moreover, Bradley and Houser (2009) found that seagrass meadows effectively attenuate wave energy, with the attenuation varying based on wave frequency and seagrass blade dynamics. In-situ and laboratory experiments suggest that vegetation cover reduces the impact of boat wakes (Bilkovic, 2017); however, previous studies have not quantified the wake attenuation capacity specifically for random waves, such as wakes, or the associated standing biomass of the vegetation. This highlights the pressing need to understand and quantify the capacity of salt marshes to dampen boat wakes, thereby advancing their application in sustainable coastal protection strategies.

1.2. Aim and objectives

The aim of this study is to investigate the role of wetlands vegetation in dissipating random wave energy. The research has two primary objectives. Firstly, it evaluates the effectiveness of vegetation in reducing wave energy, using field measurements to analyze how various vegetation characteristics, such as density and height influence this attenuation. These findings enhance the understanding of the physical mechanisms through which salt marshes mitigate wave impacts, particularly from boat wake, and highlight their potential as natural coastal defenses. Secondly, the study employs numerical model to predict wake attenuation by salt marshes under three distinct scenarios, increased boat traffic, varying vegetation density, and differing platform geometry, with the aim of quantifying the relative influence of each factor on wave attenuation

and identifying the most significant driver of wave energy dissipation. Such analysis will aid in identifying inconsistencies in current understanding of salt marsh dynamics and offer recommendations for future restoration plan.

II. State of the art

2.1. Wetland properties and ecosystem services

Wetlands are among the most ecologically valuable ecosystems, providing a wide range of essential services that benefit both the environment and human society. These vital services, as outlined in the Millennium Ecosystem Assessment (Reid et al., 2005), can be broadly categorized into four groups: provisioning, regulating, cultural, and supporting services. Provisioning services include the supply of resources such as water, fish, and plant materials, which are vital for human survival and economic activities (Reid et al., 2005). Regulating services encompass the ability of wetlands to moderate climate change by controlling water quality, regulating water flow, and mitigating flooding, while cultural services reflect the value of wetlands for recreation, education, and spiritual purposes (Reid et al., 2005). Supporting services, such as nutrient cycling, habitat provision, and biodiversity conservation, underpin the functioning of all other ecosystem services, ensuring the health and sustainability of both the wetlands themselves and the surrounding environment (Reid et al., 2005).

Wetlands have been recognized as valuable NbS to combat the negative effects of wakes and waves through their natural ability to wave energy reduction. Barman et al. (2024) studied the potential of wetlands as nature-based solutions (NbS) for promoting sustainable built environments. The authors emphasized the multifunctionality of wetlands vegetation, which provide essential ecosystem services such as water purification, flood regulation, and carbon sequestration. The review underscored the ecological and socio-economic benefits of integrating wetlands into urban planning, particularly in reducing flood risks, and supporting biodiversity. Besides, Irish et al. (2008) highlighted the aspects of coastal wetlands, including low and high marshes along U.S. coasts, composed of plant species of *Spartina alterniflora* and *Spartina patens,* playing the role to attenuate wave height and controlling flow. Additionally, Costanza et al. (2008) emphasized the significant role coastal wetlands play in mitigating hurricane damage,

providing substantial economic and ecological benefits. Using data from 34 major hurricanes in the U.S. since 1980, the researchers developed a regression model to examine the relationship between hurricane-induced damages, wetland area, and wind speed. The model revealed that increasing wetland areas significantly reduces storm-related economic damages, with a loss of 1 hectare of wetlands correlating to an average increase of $33,000 in storm damages. This emphasized the protective function of wetlands, which dissipate wave energy and reduce storm surge impacts. Similarly, Smolders et al. (2015) highlighted wetland properties such as elevation, size, and location influence their ability to mitigate flood risk. Using numerical modeling focused on the Scheldt estuary in Belgium and the Netherlands, the researchers found that wetland properties, including elevation, surface area, and location, significantly influence their ability to attenuate high water levels. Despite the multifunctionality of wetlands are well-documented, further research is needed to address gaps in understanding their effectiveness in lessening boat wake energy and protect shorelines.

2.2. Ecological succession of wetlands

Ecological succession is a natural process through which ecosystems evolve over time, driven by interactions among organisms, environmental conditions, and disturbances (Glenn-Lewin, 1992). In coastal wetlands, this succession process is particularly dynamic due to interplay of tidal regimes, salinity gradients, and sediment deposition (Glenn-Lewin, 1992). Wetland ecosystems, including tidal flats, low marshes, and high marshes, provide an example of ecological succession influenced by hydrological and biogeochemical factors (Glenn-Lewin, 1992).

Tidal flats, located at the boundary between terrestrial and marine environments, represent the initial stage of ecological succession in wetlands (Figure 1). Frequently submerged during tidal cycles, these areas are predominantly unvegetated, with landscapes shaped by sediment deposition. High salinity and frequent inundation limit plant establishment in tidal flat (Silvestri, 2005). As conditions improve through sediment accumulation and soil stabilization, tidal flats transition into low marsh zones which are regularly flooded by tidal water (Figure 1). This stage is marked by the establishment of salt-tolerant plants like *Spartina alterniflora*, which drive

further ecological development. According to Mitsch and Gosselink (2015), these plants not only stabilize the substrate but also modify the microenvironment by reducing water flow velocity and enhancing soil aeration. The tidal regime plays a pivotal role, as the frequency and duration of flooding create zonation patterns that influence species distribution (Silvestri, 2005). The low marsh thus serves as a critical transition zone, balancing between aquatic and terrestrial influences. Meanwhile, the continued accumulation of organic material and elevation gain over time lead to the development of high marsh zones (Figure 1). These areas are characterized by reduced flooding frequency, lower salinity levels, and a more diverse plant community, including species such as *Spartina patens* and *Juncus gerardii*. Chapman (2016) identified high marshes as a stable successional stage where reduced tidal influence fosters complex ecological interactions and enhances biodiversity. This progression from tidal flat to high marsh is shaped by external factors like tidal amplitude, sediment supply, and climatic conditions, with feedback mechanisms as described by Silvestri (2005), presented how vegetation influences tidal hydrodynamics and sediment deposition, reinforcing salt marsh zonation patterns. Thus, this interconnected terrains (e.g. tidal flats, low and high marshes) form a cohesive system that stabilizes coastlines, provides robust coastal protection, and delivers essential ecosystem services (Mitsch and Gosselink, 2015). This similar terrain is found in the Ria Formosa lagoon, highlighting the need for this study to quantify the effectiveness of tidal flats and low marshes in mitigating the impact of boat wakes and support future coastal management plan.

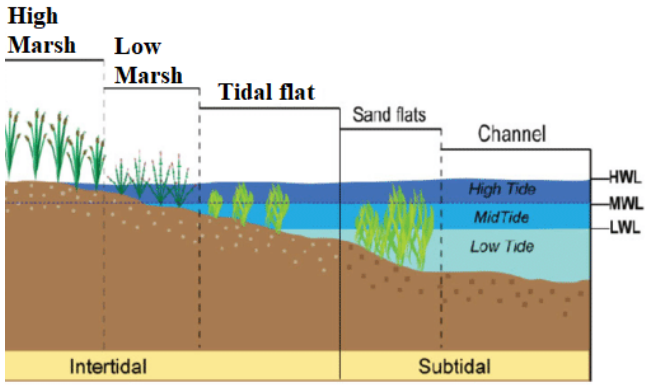

Figure 1. Pictographic view of ecological succession of coastal wetland (modified from

Taramelli et al. (2021)). HWL, MWL and LWL stands for high, mid and low water level.

2.3. Wave attenuation by vegetation

The effectiveness of salt marshes to lessen wave energy was studied across variable environmental conditions in earlier studies. Fonseca and Cahalan (1992) found that seagrass species, particularly *Thalassia testudinum*, provided the highest wave attenuation (50-70%), with denser beds offering superior protection, while *Zostera marina* provided moderate reductions, highlighting species-specific characteristics. Macro-tidal salt marshes could reduce wave heights by up to 80%, with vegetation density and marsh edge type as key factors (Möller and Spencer, 2002). Erosional edges of marsh patches with dense vegetation showed the highest wave attenuation, whereas accretional edges were less effective. Similarly, Möller et al. (2014) found wave reductions based on field study of up to 80% in dense *Spartina* vegetation, with seasonal variations in vegetation density influencing dissipation rates, which were higher during the growing season. Anderson and Smith (2014) explored the role of flexible, idealized salt marsh vegetation in wave attenuation, finding that taller, more flexible plants reduced wave heights by 10-60%. Vuik et al. (2016) examined vegetated marsh foreshores in reducing wave energy on coastal dikes, reporting reductions of 20-60% depending on vegetation type and density, emphasizing their role in coastal defense. These variations on average wave attenuation across different studies is due to plant geometry and hydrodynamic conditions (Bradley and Houser, 2009).

Wave attenuation occurs through the drag force exerted on vegetation stems, depending on both vegetation and hydrodynamic characteristics (Augustin et al., 2009). Vegetation possesses physical structures that extend above and below the water surface, creating obstacles to water flow. As water moves through these biotic structures, it encounters stems, leaves, and other parts, causing flow separation and the formation of eddies and vortices downstream. These flow disruptions generate areas of lower pressure behind the vegetation, increasing drag. Maximum drag and wave attenuation occur when vegetation reaches or extends above the water surface,

while submerged vegetation, such as seagrass, exhibits less drag and attenuation (Augustin et al., 2009; Bradley and Houser, 2009). However, submerged parts of vegetation still contribute to resistance, with denser vegetation arrangements further amplifying drag through interference in water flow patterns (Nepf and Ghisalberti, 2008).

Paul and Amos (2011) studied on *Zostera noltei*, demonstrated that a minimum stem density is required for wave attenuation, suggesting a nonlinear relationship between stem density and attenuation. They also found that this threshold varies with hydrodynamic conditions, as longer wave periods reduced the shoot density needed for attenuation. Dense vegetation, such as salt marshes and mangroves, is generally more effective at dissipating wave energy compared to sparse or short vegetation. However, seagrasses, kelp, and algae, growing underwater, can substantially reduce wave energy due to complex flow interactions with their structures (Grizzle et al., 1996). Studies on unidirectional flow suggest that interactions between vegetation stems also influence overall resistance. For instance, variations in the spatial coverage and geometry of vegetation fields can alter their attenuation capacity (Irish et al., 2008).

Collectively, these studies underscore the importance of vegetation characteristics, including species type, density, flexibility, and seasonal changes, in mitigating wave energy. However, despite these findings, a significant research gap exists in quantifying the attenuation of boat wakes. While previous research focuses primarily on natural wave dynamics, the unique characteristics of boat wake energy and the influence of species-specific density and platform geometry, remain underexplored. Addressing this gap is essential for coastal management plan.

2.4. Drag force

Dalrymple et al. (1984) first introduced drag force (F_d) as a critical force to quantify the wave energy attenuation produced by vegetation. This study revealed that drag force arises when fluid exerts resistive force on an object moving relative to it, and thus interaction is pivotal in understanding energy dissipation mechanism. The drag force equation was formulated by Dalrymple et al. (1984) in equation 1.

$$F_d = \frac{1}{2} \rho \, C_D \, A_v \, u \, |u| \qquad \text{Equation 1}$$

where, C_D is the drag coefficient, ρ is the density of the water, A_v represents the vegetation frontal area per unit volume and $|u|$ is the flow velocity. By considering the work done by this force,, Dalrymple et al. (1984) quantified energy dissipation caused by vegetation, idealizing the vegetation elements as cylinders. Moreover, this drag force based approach was further utilized by Méndez et al. (1999) to study interaction between water motion and the physical structure of vegetation. This force arises as water flows around vegetation stems, leaves, and other elements, creating turbulence and energy dissipation, which contribute to wave attenuation. In this study, drag force was used as a central concept to quantify the hydrodynamic effects of vegetation on wave attenuation. For random waves, wave attenuation equation was developed by Mendez and Losada (2004), where wave attenuation governed by the balance of wave energy flux, incorporates both the energy dissipation due to vegetation and the wave breaking process. To predict the wave height ($H(x)$) at a distance x as waves travel through vegetation, Mendez and Losada (2004) incorporate the attenuation coefficient (β), which accounts for the cumulative effect of vegetation characteristics and wave dynamics. The relationship of wave height decay is derived by Mendez and Losada (2004) resulting in equation 2.

$$\frac{H_{rms}}{H_{rms\,in}} = \frac{1}{1+\beta X} \qquad \text{Equation 2}$$

with,

$$\beta = \frac{d\,N\,k\,H_{rms\,in}}{3\sqrt{\pi}} \frac{sinh^3 kh_v + 3\,sinh\,kh_v}{(sinh\,2kh + 2kh)\,sinh\,kh} C_D \qquad \text{Equation 3}$$

where, H_{rms}, $H_{rms\,in}$ denotes root mean square wave height for random waves and incident wave respectively, β is wave damping coefficient, d is stem diameter, N is number of stems per square meter, h is water depth, k is wave number and h_v is vegetation height. The position along the transect is represented by X, with $X = 0$ at the leading edge of the vegetation field.

The SWAN (Simulating WAves Nearshore) model, developed by Booij et al. (1999), is a widely

used third-generation spectral wave model designed to simulate the transformation of wind-generated waves in coastal regions. It solves the action balance equation, accounting for processes such as wave generation by wind, propagation (refraction, shoaling), and various dissipation mechanisms, including white-capping, bottom friction, and depth-induced breaking. An important extension to SWAN has been the inclusion of wave energy dissipation due to vegetation, particularly using a drag force-based approach (Suzuki et al., 2012), which has proven effective in representing the attenuation capacity of natural systems such as mangrove forests and vegetated foreshores (Vuik et al., 2016).

The drag force-based approach, introduced into SWAN by Suzuki et al. (2012), models vegetation as rigid cylinders that exert hydrodynamic drag on wave-induced orbital velocities, thereby adding vegetation-induced energy loss as an additional dissipation term in the wave action balance equation. This drag is typically parameterized using a bulk drag coefficient, vegetation density, diameter, and height, and the formulation is depth-dependent to capture the layered structure of vegetation. This allowed SWAN to simulate vegetation-induced wave damping with spatial and vertical resolution, accommodating tidal variability and plant morphology. This model was expanded by Lopez-Arias et al. (2024), who developed a species-specific drag coefficient formulation for mangroves (*Rhizophora sp.*). Their formula improves the predictive capability of SWAN by accounting for plant-specific morphology and hydrodynamic context.

The integration of drag force-based vegetation modeling into SWAN is especially valuable for designing and evaluating nature-based solutions (NbS). Vuik et al. (2016) used this approach to quantify how vegetated foreshores reduce wave energy on coastal dikes. Their results showed that strategic implementation of vegetation can lead to significant wave attenuation, decreasing structural design loads and improving coastal resilience. Compared to purely empirical models like that of Mendez and Losada (2004), the drag-based method within SWAN offers more flexibility in simulating future scenarios, including vegetation degradation or restoration.

So, the flexibility of SWAN to incorporate vegetation-induced dissipation through a drag force-

based term enhances its capability to model wave attenuation in vegetated coastal zones. This method is physically robust, site-specific, and aligns well with the needs of coastal engineers and planners aiming to implement resilient, nature-based coastal protection. sustainable coastal protection systems.

The present study aims to quantify boat wake attenuation due to vegetation and platform geometry within a specific coastal wetland using the SWAN model. Utilizing a drag force-based approach, SWAN is applied to simulate a range of scenarios involving varying boat wakes, vegetation density and platform geometry. Realistic vegetation characteristics and site-specific topographic data are incorporated to explore the influence of vegetation on wave energy dissipation. The SWAN model is calibrated using in-situ wave evolution data to ensure reliable representation of wave decay across the study site. This scenario-based modeling framework effectively links detailed hydrodynamic processes with large-scale wave simulation, providing valuable insights into the role of salt marshes in attenuating boat wake energy. The findings contribute to a deeper understanding of protective function of coastal wetlands and support informed decision-making for sustainable coastal management in regions exposed to frequent boat traffic.

III. Study site

The study site is a wetland area along the Ramalhete channel located in the western part of Ria Formosa lagoon, a mesotidal lagoon system in southern Portugal (Figure 2 a). The lagoon spans 55 km along the coastline of southern Portugal and connects to ocean through seven tidal inlets, where 90% of water exchange between lagoon system and sea in tidal cycle are governed by Ancão, Faro-Olhão, and Armona inlets as shown in Figure 2(a) (Pacheco et al., 2010). At the Faro-Olhão Inlet, the flood prism is significantly larger than the ebb prism, accounting for approximately 8% during spring tides and 12% during neap tides (Pacheco et al., 2010). Conversely, the Armona Inlet consistently exhibits ebb dominance (Pacheco et al., 2010). There is a significant residual water circulation, especially from the Faro-Olhão Inlet towards the Ancão and Armona inlets (Ferreira et al., 2016). The Ramalhete Channel, which links the Faro-Olhão and Ancão inlets, experiences strong tidal asymmetry, with shifts in dominance between flood and ebb tides (Ferreira et al., 2016). The lagoon experiences semi-diurnal tidal cycle with neap tidal range of about 2 m, which increases to 3.5 m during spring tide (Ferreira et al., 2016; Kumar et al., 2020). Offshore waves are restricted to this site (Carrasco et al., 2018), and primary driver of water circulation is due to tidal movement (Salles, 2001).

Due to sheltered position of the study site in the Ramalhete channel, waves are mainly associated with touristic or fisheries boat wake which propagates towards the salt marshes of this region (Newton et al., 2022). The lagoon consists of salt marshes and tidal flat, both vegetated and non-vegetated region, accounting for more than two-third of the total lagoon area. This lagoon, spanning approximately 1304 ha of intertidal area, hosts foremost species of *Spartina maritima*, *Sarcocornia perennis* and the seagrass *Zostera noltei* (Santos et al., 2019). This lagoon is a significant ecosystem and a valuable resource for the region, supporting tourism, fisheries, aquaculture, and salt extraction industries (Newton et al., 2022). This coastal lagoon is known for its biodiversity and its role in sustaining local economies through these various activities (Newton et al., 2022).

To study wave dynamics in this environment, three different profiles, S1, S2 and S3, over study site in Figure 2 (b) are shown in Figure 3 as a schematic diagram. The location of profiles was varied in length, platform width, elevation, slope, species, and vegetation cover. Vegetated areas with diverse plant communities were sampled across various profiles from low marsh to tidal flat, *with Spartina maritima* and *Zostera noltei* present at both S1 and S2, while S3 was non-vegetated. This study is conducted up to the low marsh, as it is frequently submerged providing insight into the level of wave attenuation, generated in the Ramalhete channel, and propagated toward the lower marsh.

Figure 2. (a) Location of study site at Ria Formosa lagoon collected from google satellite map (Google Earth. (2024). Satellite imagery of Ria Formosa Lagoon, Portugal. Imagery provider: Airbus. Retrieved November 23, 2024); and (b) Zoom in view of study site with three different profile S1, S2 and S3 as red color straight line, location of PTs deployment, sediment and biomass sample collection are marked as blue and yellow circle marked, respectively.

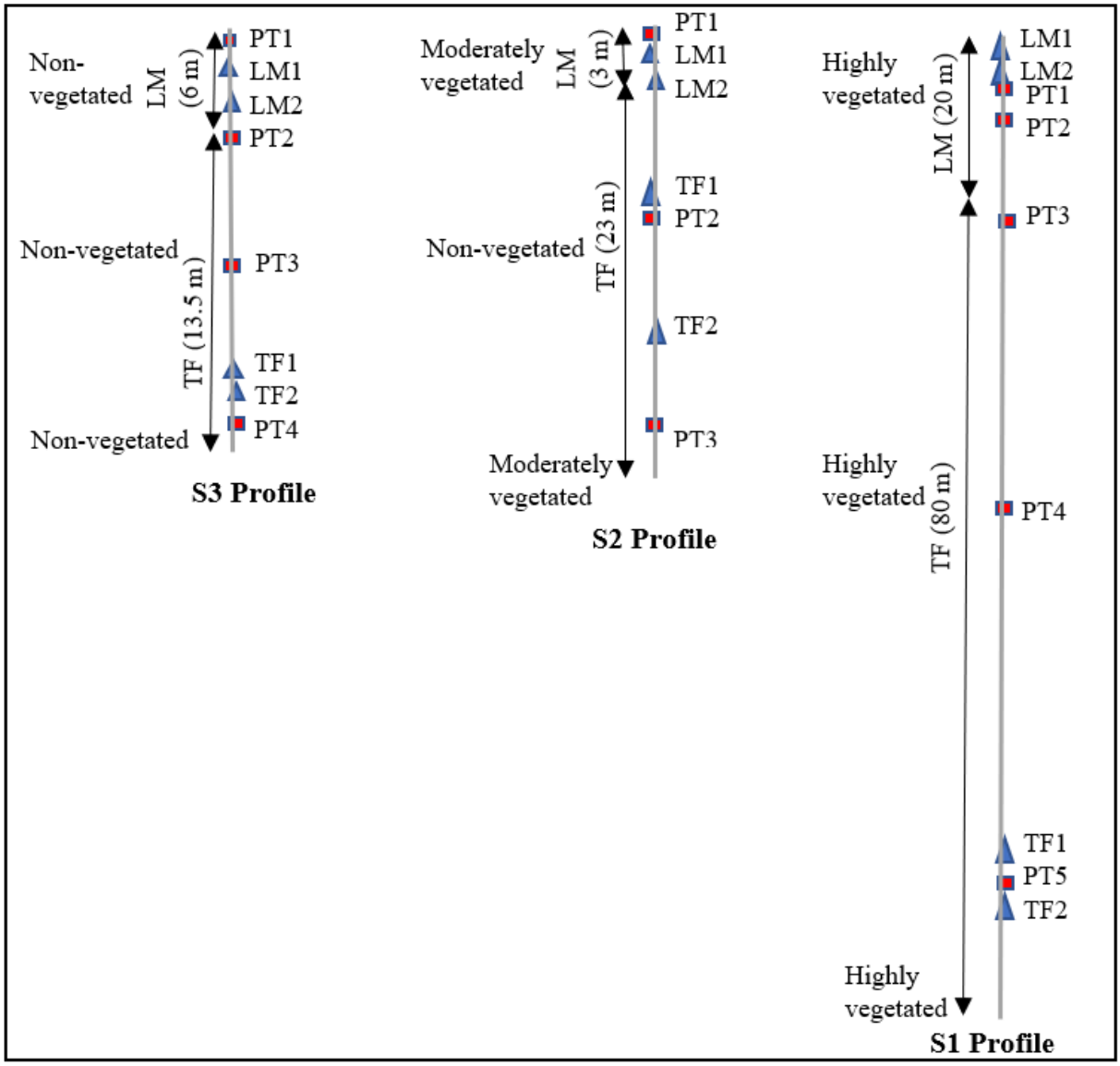

Figure 3. Schematic diagram of three profiles (light black color straight line), S1, S2 and S3 with sampling (blue triangle) and PTs deployment (red square) locations.

IV. Methodology

4.1. Fieldwork data collection

The fieldwork campaigns took place between October 15th and November 5th, 2024, and included the collection of ecological metrics, sediment and topographic data, and hydrodynamic data (Figure 4). The objectives of the fieldwork campaigns were threefold. Firstly, to collect ecological characteristics of the wetland habitats, such as leaf length, leaf diameter, standing biomass, and plant coverage. Secondly, to acquire information on sediment grain size characteristics and local elevation of each profile. Third, to collect data on water levels, assessing boat wake attenuation and propagation, after generation in the Ramalhete channel. Fieldwork was strategically planned to coincide with low tide conditions for ecological data collection, sediment sampling and topographic survey, and for the equipment deployment; and with high tide periods to generate boat wakes.

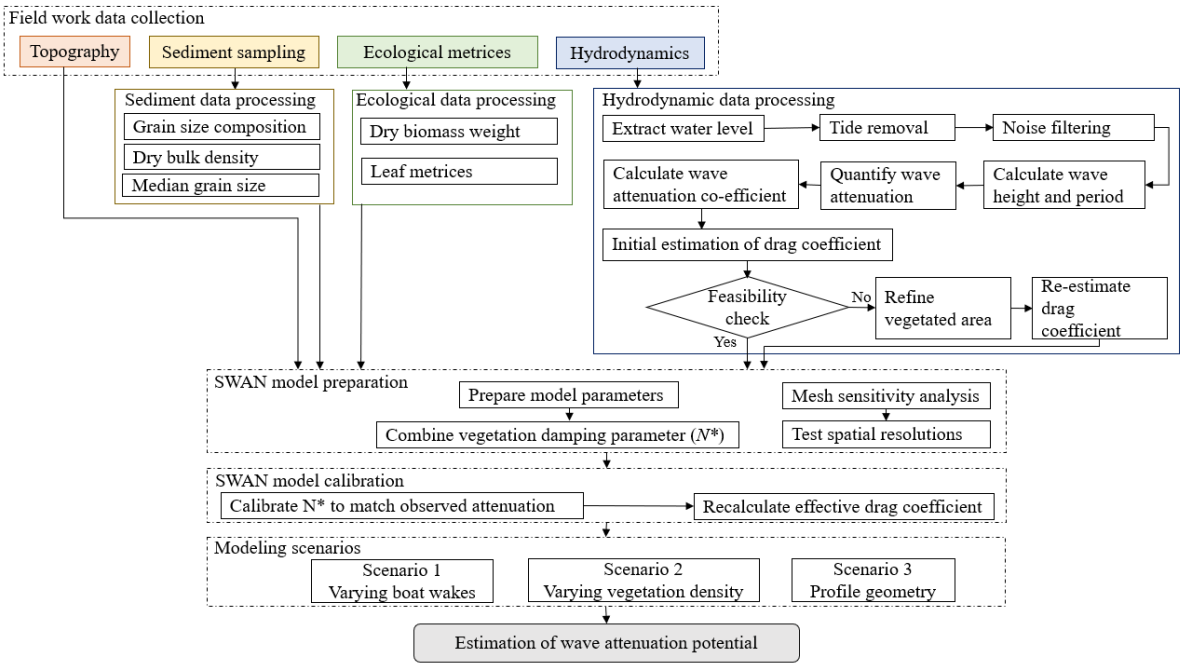

Figure 4. Approach to quantify the influence of wave attenuation processes from the field data collection until the final modelling scenarios.

4.1.1. Ecological data collection and sediment sampling

Prior to ecological metrics data collection, species identification was conducted. Subsequently, ecological measurements were carried out along each surveyed profile, oriented perpendicular to the channel. A total of four sampling locations per profile were collected to capture representative data in each profile (Figure 3). The biomass sampling method followed the procedure described in earlier research by Howard et al. (2014). The method involved defining sampling areas with quadrats of 30 cm × 30 cm (Figure 5a). Within each quadrat, the overall vegetation coverage, stem density, and the mean leaf diameter and length, of 5 replicate per species were measured (Figure 5b). To estimate above-ground biomass, at least 50 randomly selected stems within a quadrat were cut above ground (Figure 5c), transferred into plastic bags, and taken into the laboratory. Additionally, near the location where biomass data was collected, approximately 50 cm^3 of sediment was extracted using plastic syringes, transferred into plastic cups (Figure 5d), and then transported to the laboratory. All collected samples were marked with different labelling, such as for Low Marsh (LM) as LM1, LM 2, and for Tidal Flat (TF) as TF1, TF2 (Figure 3 in section 3). Such labelling helped the sample to be easily identified, systematically handled and distinguished from others.

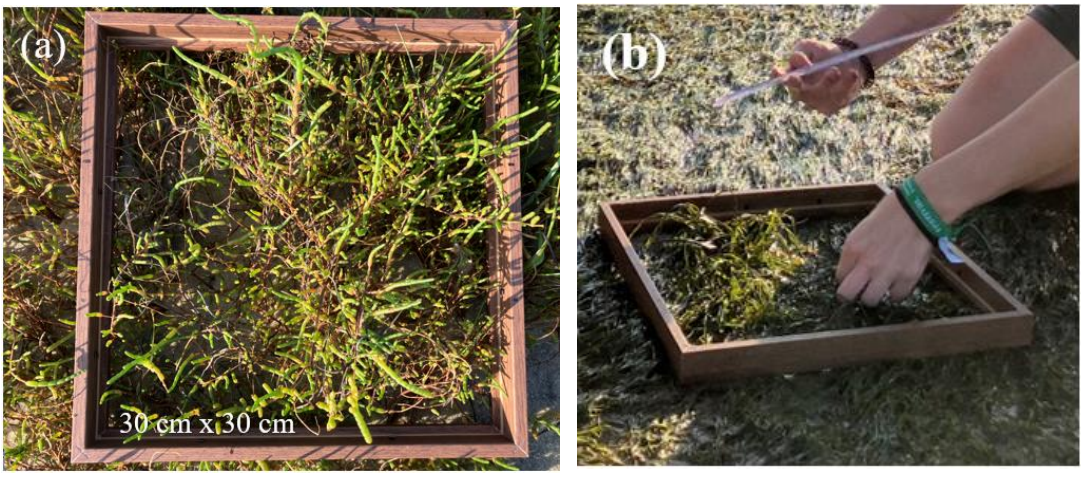

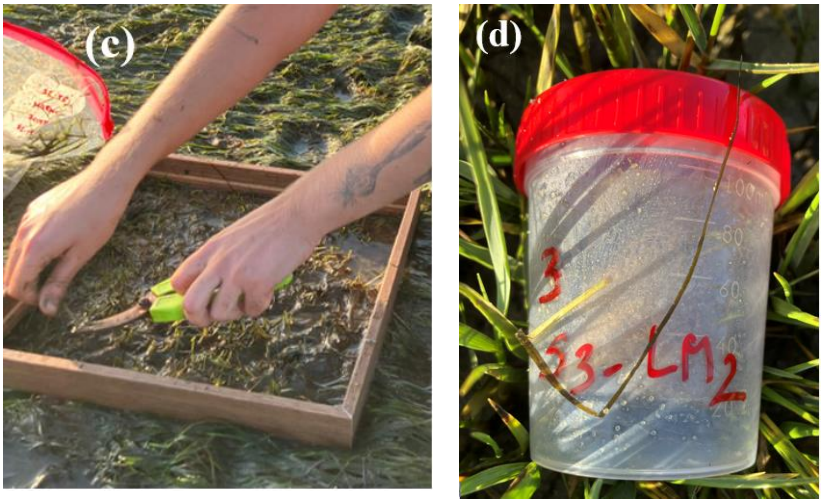

Figure 5. View of (a) low marsh sampling station on profile S2, as an example of the 30 cm × 30 cm sampling quadrat area, used for above-ground biomass data collection, (b) measurements of plant height, diameter and plant coverage within the quadrat in the tidal flat, (c) chopping down of the above-ground biomass in the tidal flat, and (d) plastic cup used to store the sediment sample.

4.1.2. Topography data collection and hydrodynamics

The topography of the surveyed profiles was obtained during low-tide conditions, using real-time kinematic Differential Global Navigation Satellite System (RTK-DGNSS; with a horizontal and vertical accuracy of 0.01 m and 0.02 m, respectively) surveying along three profiles of S1, S2 and S3, perpendicular to the Ramalhate channel. Data was recorded with a 1-second interim time. The locations where the biomass and the sediment data were collected, were positioned with the RTK-DGNSS.

Pressure Transducers (PTs), at sampling frequency of 4 Hz, were deployed 2 cm above ground level (Figure 6) during low tide, in the surveyed profiles: five locations on S1, three on S2, and four on S3 profile. The PTs were distributed from the edge of the low marsh towards the tidal flat, and labelled as PT1, PT2, PT3, PT4, and PT5 (Figure 3 in section 3). PTs were placed within

areas of relatively homogeneous vegetation and topography, ensuring that each was located within a consistent and representative ecological zone. PTs locations were also recorded with RTK-DGNSS. Boat wakes were generated during high tide when all PTs were submerged. The boat was moving alongshore the channel (cross-shore to the monitored profiles), about 20 meters from the study area. The boat was traveling at fixed velocities of 8, 10, and 12 knots, each for 10 repetitions, with varying directions from east to west and west to east. Multiple runs ensure consistent generation of wake patterns at each velocity. The waves generated by boat wakes were naturally propagated into the studied wetland platform without any further human interaction.

Figure 6. Installation of a Pressure transducer (PT) to measure water depth (example of deployment at the low marsh in S2 profile).

4.2. Laboratory analysis and data postprocessing

4.2.1. Ecological and sediment data analysis

The dry weight of above-ground biomass (g/cm^2) was estimated based on 50 collected stems, which were oven-dried at 60°C for approximately 72 hours until reaching a constant weight (Figure 4).

Sediment samples were prepared to analyze water content (H_2O%) and median sediment grain size (d_{50}) (Figure 4). To determine water content and dry bulk density, wet samples were weighed and then dried using the same procedure. The water content was calculated as the proportion of weight lost after drying, relative to the initial wet weight, while the dry bulk density was derived from the dry weight divided by the known volume of each sample.

Wet sieving and laser diffraction were used to assess the grain size of the fine and coarse sediment fractions of the collected samples. The sieving was performed by placing a 2 mm sieve on a collector pan with an outlet, and the samples were sieved by pouring them over the sieve and adding deionized water, allowing the fine fraction to be collected in the pan. To determine the particle size distribution of the finer sediment fraction (<2 mm), a laser diffraction analysis was performed using a Malvern Mastersizer 3000 (Malvern Instruments Ltd., Worcestershire, UK). Before, a pre-treatment with hydrogen peroxide to oxidize organic content and dispersant to break up aggregates was conducted (Figure 7). Malvern Mastersizer 3000 calculated particle size by measuring blue and red band laser light intensity variations, as it passes through a particle suspension, with diffraction angle and intensity indicating particle size and quantity (Figure 7). Optimal operating settings, such as stirring rate, measurement time, and obscuration level (5-30%) were tailored to sample composition. Each sample was measured six times, with background checks confirming system cleanliness. The grain size distribution and statistical parameters for all collected samples, including the mean diameter (d_{50}), were computed using GRADISTAT v.8.0 (Blott and Pye, 2001).

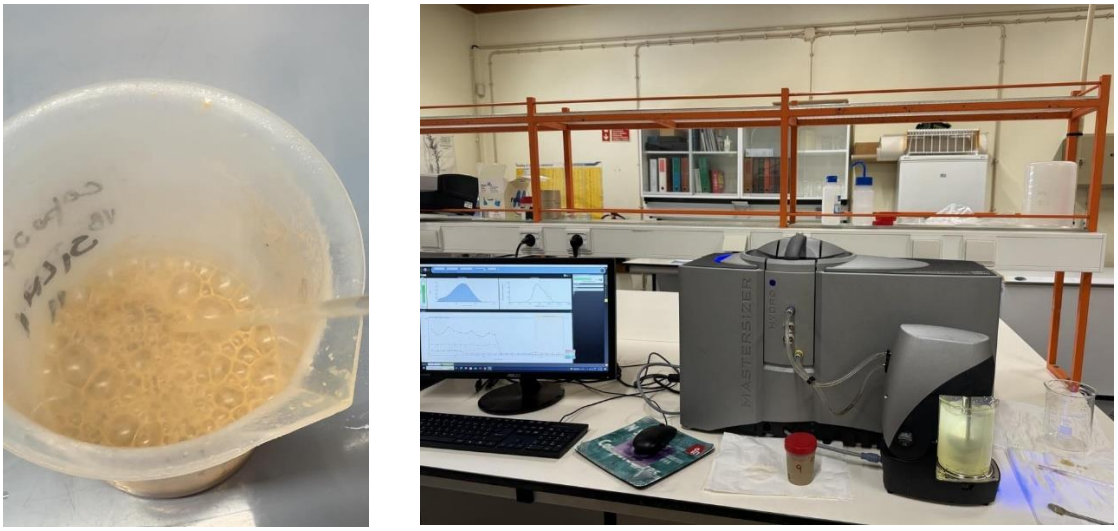

Figure 7. Pre-treatment of fine sediment with hydrogen peroxide (left panel) and view of the Malvern Mastersizer 3000 (right panel).

4.2.2. Topography and hydrodynamics data analysis

The elevation gradient (slope) between consecutive PTs was also calculated. Water depth information was extracted from the PTs recorded file (Figure 4). To focus on dynamic water levels, a moving average detrending approach was initially applied to remove tidal effects (Figure 4). However, recorded water level variations corresponding to different boat speeds exhibit substantial noise, likely caused by local wind-generated waves or the influence of other passing boats, such as ferries, during the field campaign (see Figures A1 - A3 in the Appendix). To address this, a filtering threshold of 1.5 times the standard deviation of the recorded water level was selected (Figure 4). This parameter was found to be optimal, as it retains a greater number of coherent wave groups compared to other tested thresholds. Specifically, filtering with the 1.5 factor consistently revealed the expected 10 wave groups, aligning with the 10 boat laps conducted during data collection (see Figures A4 – A6 in the Appendix). In contrast, a threshold, such as a factor of 2, resulted in the omission of several wave groups and yields shorter, less coherent sequences. Such omissions compromised the integrity of the wave analysis. Therefore, the 1.5 filtering factor was adopted for all subsequent calculations, as it provides a more accurate

and representative representation of waves based on empirical observations (see Figures A4 - A6 in the Appendix).

Wave height, period, and wave number were then calculated using the zero up-crossing technique (Figure 4) (Tucker and Pitt, 2001). Since wave energy is proportional to the square of wave height (H^2), the percentage of energy dissipation between two consecutive PTs was calculated using equation (4) to assess wave energy attenuation along profile.

$$\text{Dissipation (\%)} = \frac{H_{rms,o}^2 - H_{rms,f}^2}{H_{rms,o}^2} \times 100 \qquad \text{Equation 4}$$

where $H_{rms,o}$ is the root mean square wave height measured at the more seaward PT (outer PT) and $H_{rms,f}$ represents the measured root mean square wave height at each landward PT along the profile, with f denoting the PT number. Wave dissipation was determined sequentially across the profile, providing a clear evaluation of overall wave energy dissipation potential, as the wave propagates landward. Additionally, the wave attenuation coefficient (β) was determined by fitting equation (2) (refer to Section 2.4) to the obtained in situ wave height data, by considering the wave heights in the tidal flat edge, near the channel (outer PT), as the incident waves (Figure 4).

4.3. Numerical modelling

4.3.1. Model setup

SWAN model was applied in a one-dimensional (1D) scheme, per surveyed profile, to assess wave attenuation based on the drag coefficient-based approach. The model setup incorporated the collected field data as topographic data, detailed vegetation characteristics, and water depths, to capture the spatial variability of wave-vegetation interactions (Figure 4). Sediment type, either muddy or sandy, was integrated by specifying appropriate bottom friction parameters, enhancing the model's realism in simulating wave energy dissipation (Figure 4). For muddy substrates, a MADSEN friction coefficient of 0.02 was applied, while sandy substrates used a JONSWAP

friction coefficient of 0.02. A wave breaker parameter of 0.65 was also included to account for wave-breaking processes. Wave input data consisted of significant wave height (H_s) and mean wave period (T_{mean}), measured at PT5 for profile S1, PT3 for profile S2, and PT4 for profile S3, providing accurate boundary conditions for simulation of wave attenuation across different profiles. Although analytical formulations for wave attenuation are traditionally expressed as a function of root mean square wave height (H_{rms}), in this study, the model is directly driven by H_s obtained from field data. Since H_s cannot be reliably transformed into H_{rms} using a standard Rayleigh distribution, this study focuses on the observed evolution of H_s along the profile to quantify potential wave attenuation.

4.3.2. Mesh sensitivity test

A mesh sensitivity analysis was conducted to assess the impact of grid resolution on model accuracy (Figure 4). Different spatial resolutions were tested to ensure that wave transformation processes, particularly wave attenuation was adequately captured. The selected mesh resolution was a balance between computational efficiency and spatial accuracy, ensuring that results were not artifacts of overly coarse or overly refined grids.

To assess the influence of spatial resolution on the wave attenuation process, a sensitivity analysis was conducted in SWAN using diverse grid configurations, defined by the number of computational cells per wavelength, for the boat velocity of 12 knots. The model performance across the surveyed profiles (S1, S2, and S3) with in situ measurements overlaid for validation. Each profile compared significant wave height (H_s), wavelength to depth ratio (L/h), non-dimensional wave height (H_s/h), and wave steepness (H_s/L) across distance. The analysis was performed to define the optimal grid resolution to be used for all SWAN simulations (see section 5.3).

4.3.3. Drag coefficient estimation

Initial estimations of drag coefficient (C_D) were obtained using the in-situ wave attenuation

coefficient (β) within the wave damping equation presented in equation (3) (refer to Section 2.4) (Figure 4). This equation incorporates a damping coefficient (β), which is influenced by wave characteristics, vegetation properties, and the drag coefficient (C_D). With known vegetation parameters and wave conditions, the relationship between wave attenuation coefficient (β) and drag coefficient (C_D) provided a basis for estimating drag values. This reference condition adopted the entire cross-shore topography (for the three surveyed profiles), which included both the lower marsh (LM) and tidal flat (TF), as a unified zone. However, this yielded unrealistically high drag coefficient (C_D) values (often exceeding 100) that were not physically plausible. To address such shortcomings, the analysis was refined to focus specifically on individual zonation separately, where damping was expected (Figure 4). This yielded a more reasonable estimation for the drag coefficient (C_D), suitable for SWAN input.

4.3.4. Model calibration

Incorporating vegetation effects into SWAN model required specifying parameters such as the drag coefficient (C_D) and vegetation parameters. However, a key limitation of the SWAN framework is that these parameters, besides the vegetation density (N), must be defined as constant values across the entire vegetated transect, i.e., spatial variability for the other variables at the cell level is not supported. To address such constraint, a combined vegetation damping parameter (N*) was used (Figure 4), defined in equation (5).

$$N^* = C_D \times d \times h_v \times N \qquad \text{Equation 5}$$

where, d denotes the stem diameter, N represents the stem density per square meter, and h_v refers to the vegetation height. This N* was considered instead of N to include special variability along the transect. To calibrate the model for wave attenuation, vegetation parameters and drag coefficient (C_D) were initially set to a unit value. The combined vegetation damping parameter (N*) was then adjusted to mimic observed wave attenuation (Figure 4). This approach allowed for flexible tuning within the model's constraints, while preserving physical realism. Once the model outputs aligned with field observations, the drag coefficient (C_D) were re-calculated from

the calibrated vegetation damping parameter (N^*) based on equation (5), for each marsh zonation, incorporating the measured stem diameter (d), vegetation height (h_v), and stem density (N) from field data. The conducted approach provided a practical solution for representing spatially variable vegetation effects within the limitations of the SWAN modelling framework.

Subsequently, the Keulegan-Carpenter number (KC) was calculated using equation (6) to characterize the flow regime around vegetation.

$$KC = \frac{U\,(z)\,T_{mean}}{d} \qquad \text{Equation 6}$$

with,

$$U\,(z) = \frac{\pi\,H_{s,o}}{T_{mean}} \cdot \frac{cosh\,(k(h-z))}{sinh\,(kh)} \qquad \text{Equation 7}$$

where $U\,(z)$ is the maximum horizontal orbital velocity, and T_{mean} denotes the mean wave period. The orbital velocity $U\,(z)$ was estimated using linear wave theory, where $H_{s,o}$ is the significant wave height at outer PT, k is the wave number ($k = 2\pi/L$), h is the water depth and $z = -h + hv$. This formulation allows for a realistic representation of near-bed flow conditions influencing vegetation drag and wave attenuation.

4.3.5. Modelling scenarios

To comprehensively assess the wave attenuation potential in coastal wetlands, three distinct modelling scenarios were implemented in the SWAN model (Figure 4). Each scenario isolates a specific influencing factor: boat wakes variability (Scenario 1), vegetation density (Scenario 2), and profile geometry (Scenario 3), with different ranges for computed the input variables within each scenario (see Table 4). This structured approach enables a clearer understanding of how individual parameters contribute to overall wave energy dissipation.

4.3.5.1. Scenario 1: Potential of attenuation of varying boat wakes using constant vegetation

To isolate the effect of varying significant wave height (H_s) on attenuation, all scenarios were run using the S1 configuration profile, with a constant wave period (T_{mean}) of 1.5 seconds, for the boat velocities of 8, 10, and 12 knots. The selected H_s (0.04, 0.08 and 0.15 meters) span the full range observed in the field, along with two empirically derived maximum H_s (0.22 and 0.41 meters) based on varying boat sizes and sailing distances as reported by Bilkovic et al. (2019). Vegetation effects were incorporated through a combined vegetation damping parameter (N*). N* values for tidal flat (dominated by *Zostera noltei*) and low marsh (dominated by *Spartina maritima*) based on C_D-KC relationship at higher wave energy conditions which denotes higher KC associated with lower C_D. Conversely, for smaller wave conditions, such as H_s of 0.04 m, lower KC values associated with higher C_D was applied to reflect reduced flow intensity around vegetation elements.

The wave attenuation rate was calculated for each vegetation zone individually, as well as for the combined presence of both species, using equation (8).

$$\text{Wave attenuation rate} = \frac{H_{s,f}}{H_{s,o}} \qquad \text{Equation 8}$$

here, $H_{s,o}$ denotes the significant wave height at outer PT, while $H_{s,f}$ represents the significant wave height at a landward PT along the profile, where f indicates the PT number, with f = 3 for the tidal flat (TF) and f = 1 for the inner most point of the low marsh (LM) in the S1 profile. This sequential approach enabled a more precise evaluation of the potential attenuation capacity of each vegetation type, with the TF dominated by *Zostera noltei* and the LM by *Spartina maritima*.

4.3.5.2. Scenario 2: Influence of vegetation density on wave attenuation

This scenario examined the influence of vegetation density on wave attenuation, using the S1 configuration profile. Baseline stem densities of 1400 shoots/m^2 for *Spartina maritima* and 4800

shoots/m^2 for *Zostera noltei,* measured in field, were complemented with stems densities from earlier research, including *Zostera noltei* densities ranging from 1000 to 7000 shoots/m^2 (Cabaço et al., 2009; Ondiviela et al., 2018) and *Spartina maritima* densities ranging from 450 to 2500 shoots/m^2 (Castellanos et al., 1998; Sánchez et al., 1997), from seagrasses and marshes in Portugal and Spain. The model incorporated varying vegetation effects through the combined vegetation parameter (N*), as described in Scenario 1, for higher H_s of 0.09 meters. For the complementary vegetation density cases, N* was recalculated using equation (5). Stem diameter (d) and height (h_v) were kept constant based on field measurements, while the drag coefficient (C_D) was selected from the C_D-KC relationship corresponding to higher KC values. Stem density (N) was chosen based on values reported in the literature.

To maintain consistency across all simulations, a representative significant wave height (H_s) of 0.09 m and period of 1.5 s were applied. The output analysis focused on the wave attenuation potential across varying density scenarios, providing a visualization of how stem density influences wave energy reduction.

4.3.5.3. Scenario 3: Influence of profile geometry on wave attenuation

The role of profile geometry in wave attenuation was investigated by comparing changes in C_D observed in the surveyed S1, S2, and S3 profiles, characterized by varying slopes. To account for elevation differences, a reference elevation section (E1-E2) was defined across all profiles, ensuring that simulations were conducted over a consistent elevation range (Figure 9). Significant wave height (H_s) and wave period (T_{mean}) were feed into the model at a uniform reference elevation (0.45 m below mean sea-level) for all profiles. The values of H_s and T_{mean} measured by the outer PT (PT3) on the S2 profile were used, as this location was closest to the defined reference elevation (Figure 9). To simplify the analysis and enhance interpretability, a constant T_{mean} of 2 seconds, representative of values recorded in the field, was used in all simulations, paired with a range of H_s, 0.05, 0.12, and 0.20 m, which reflected the observed field conditions. All profiles were subjected to identical incident wave conditions. In the reference case, which represents the vegetation conditions observed during the field campaign, the combined

vegetation parameter (N*) was included in the model. N* values were derived based on the C_D-KC relationship as outlined in Scenario 1. In this context, H_s of 0.05 m corresponds to lower KC values, while H_s values of 0.12 and 0.20 m are associated with higher KC values. In contrast, for the non-vegetated case, all vegetation parameters were removed to simulate bare conditions. To assess the effect of vegetation on wave attenuation, the difference in the wave attenuation rate ($\Delta \frac{H_{s,f}}{H_{s,o}}$) between the non-vegetated and reference cases was calculated using equation (8), where f=2 corresponds to the tidal flat (TF) and f=1 represents the innermost point of the low marsh (LM) in the S2 and S3 profiles.

V. Results

5.1. Ecology and sediment

5.1.1. Vegetation properties

The three profiles reveal distinct spatial variability between the tidal flat (TF) and low marsh (LM) zones in terms of plant species composition, coverage, stem density, and dry biomass weight (Table 1).

In the TF, *Zostera noltei* is the dominant species across all profiles, but with varying coverage. Profile S1 exhibits the most uniform and dense vegetation, with 100% coverage in all tidal flat subzones and a stem density of 4823 stems/m^2 with dry biomass ranging from 2.2 to 2.5×10^{-3} g/cm^2 (Table 1). In comparison, profile S2 displays a higher spatial variability in TF, with vegetation coverage ranging from 60% to 90% and the highest recorded stem density among all profiles at 6674 stems/m^2. However, biomass values are slightly lower, between 1.0 and 1.9 × 10^{-3} g/cm^2, suggesting potentially denser but less mature vegetation (Table 1). Profile S3, by contrast, has a non-vegetated TF.

In the LM, *Spartina maritima* is the prevalent species, denoting conspicuous arrangements among the profiles. Profile S1 maintains a 50% vegetation coverage with a stem density of 1467 stems/m^2, with the highest biomass across all sites (18.5–20.4 × 10^{-3} g/cm^2; Table 1). Profile S2 shows more variability in the LM arrangement, with vegetation coverage ranging between 20% and 60% and a slightly higher stem density of 1534 stems/m^2 with biomass values ranging from 8.3 to 17.9 × 10^{-3} g/cm^2 (Table 1), suggesting that while the plant count was high, individual plant mass or structural rigidity might have been comparatively low. Profile S3 has a non-vegetated LM.

Table 1. Vegetation characteristics across study site (TF – Tidal Flat; LM – Low Marsh).

Profile	Sample identification	Plant species	Vegetation height, h_v (m) $\times 10^{-2}$	Stem diameter d (m) $\times 10^{-2}$	Coverage (%)	Density, N (stem/m^2)	Dry biomass weight (g/cm^2) $\times 10^{-3}$
S 1	TF 1	*Z. noltei*	32.6	0.2	100	4823	2.2
	TF 2						2.5
	LM 1	*S. maritima*	32.5	1	50	1467	20.4
	LM 2						18.5
S 2	TF 1	*Z. noltei*	13.6	0.1	90	6674	1.9
	TF 2				60		1.0
	LM 1	*S. maritima*	15.1	0.4	20	1534	8.3
	LM2				60		17.9
S 3	TF 1	Non-vegetated	-	-	-	-	-
	TF 2				-		-
	LM 1	Non-vegetated	-	-	-	-	-
	LM 2				-		-

5.1.2. Sediment properties

The sediment median grain size (d_{50}) and the dry bulk density analysis revealed spatial heterogeneity across the surveyed profiles and in the four sampling locations (LM1, LM2, TF1, and TF2; Figure 8). Profile S1 represents a mixed sediment regime, comprising two distinct environments: the TF is dominated by fine sediments, with silt content ranging from 65 to 69%, whereas the LM is sand-dominated, with sand content reaching roughly 55% (Figure 8a). Clay and gravel fractions are negligible across S1 in the sampling locations. In contrast, S2 and S3 profiles are characterized by sand-dominated, with sand comprising over 74%, regardless of the sampling locations; relatively low contributions from silt, clay, and gravel were verified in S2 (Figure 8a).

In S1, LM1 and LM2 have the finest sediments with d_{50} values below 100 μm, which are

classified as very fine sand according to Blott and Pye (2012), while in S2 and S3, the low marsh had d_{50} values above 350 µm, classified as medium sand (Figure 8b). The tidal flat of S1 has finer sediments (d_{50} < 50 µm; coarse silt), while the d_{50} for TF in S2 and S3 ranges between 350 - 400 µm (medium sand), reinforcing the dominance of coarser sediments in those profiles (Figure 8b). Dry bulk density results further support this distinction. S1 exhibits significantly lower dry bulk density, typically below one (g/cm^3; Figure 8c). These lower dry bulk densities are indicative of high organic matter content, commonly associated with finer-grained sediments. However, S2 and S3 exhibit consistently higher bulk density (approximately 1.5 to 1.9 g/cm^3) across all locations, corresponding to mineral-rich sediments and dominance of coarser grain sizes (Figure 8c).

(a)

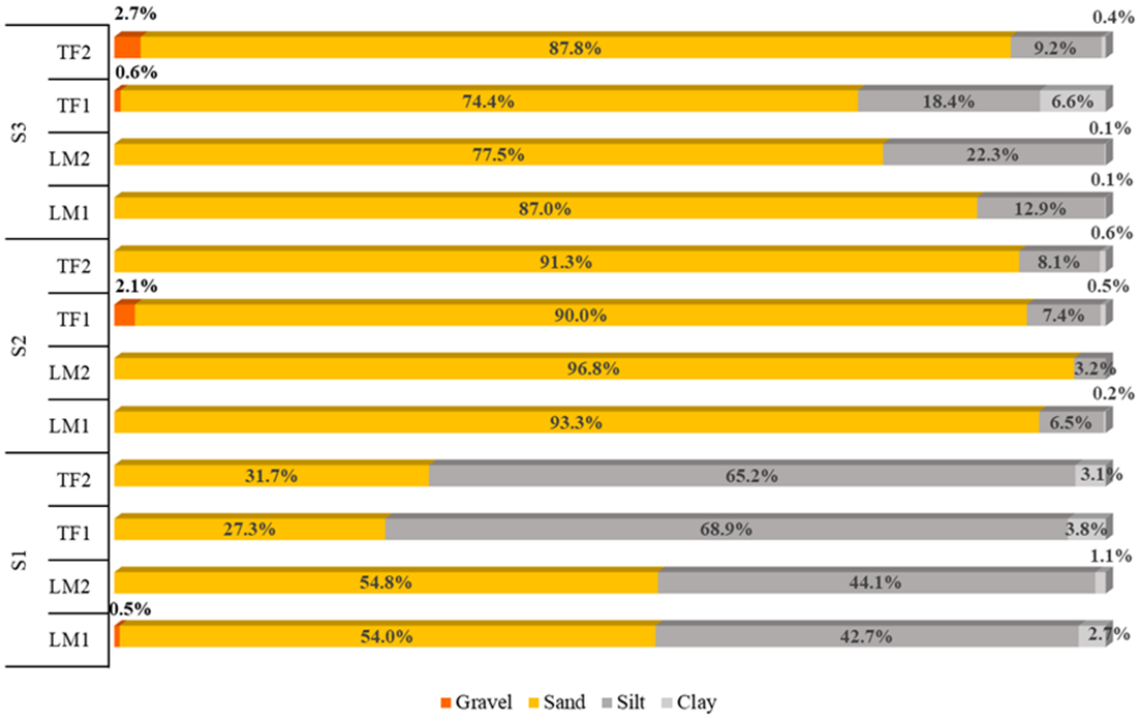

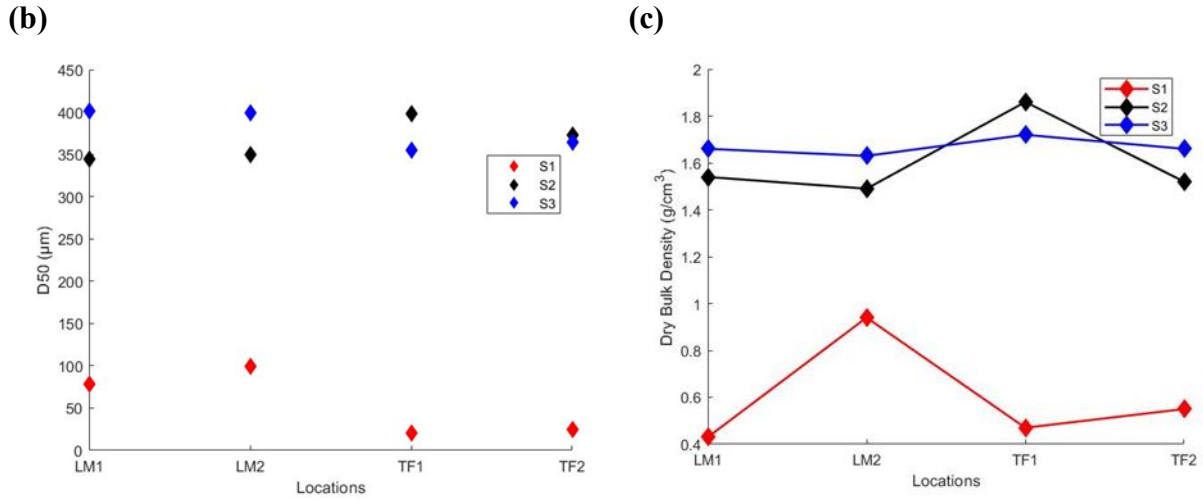

Figure 8. Spatial variation of sediment properties across LMs (Low Marsh) and TFs (Tidal Flat) in profiles S1, S2, and S3 with (a) grain size composition with distinct colour ramps for each type of sediment, (b) median grain size (d_{50}), and (c) dry bulk density.

5.2. Topography and hydrodynamics

5.2.1. Profile morphology

Profile S1 is the longest of the three, spanning approximately 100 meters (Figure 9). It features significant elevation variability, transitioning from low marsh to the tidal flat. On the contrary, profile S2, with a length of about 26 m, is shorter than S1 and displays a steady downward slope from low marsh to the tidal flat, reaching - 0.8 m Mean-Sea Level (MSL) at the channel (Figure 9). The gradient at S2 is more uniform compared to S1 (Figure 9). Profile S3 is the shortest, spanning roughly 19.5 m (Figure 9). It starts at a lower elevation (0.8 m MSL) than S2 and shows mild sloping from the LM to TF. The elevation drops to -0.8 m MSL at the channel. As a result of the different profile geometry, there is also a difference on the distance and slope of the profiles within the reference elevation zone E1-E2 (Figure 9).

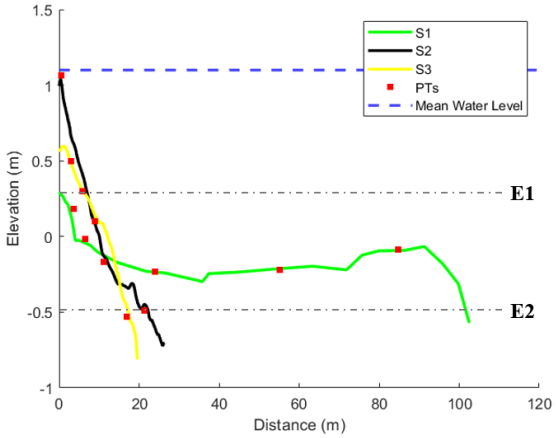

Figure 9. Elevation (referred to Mean-Sea Level, MSL) of the surveyed profiles, and pressure transducers (PTs) location (red square). The reference elevation zone E1-E2 (light black dotted horizontal lines) is also noted. The Mean Water Level blue mark of 1.1 meters that PTs remained submerged across all profiles, enabling reliable and comparable wave attenuation analysis, under consistent hydrodynamic conditions.

5.2.2. Hydrodynamics

An analysis of the cross-shore variability of each set of waves generated by the boat reveals distinct spatial patterns along the profiles (see Figures A1 – A6 in the Appendix A). For the S1 profile, the wave height decreases progressively as the waves propagate toward the landward direction, indicating energy dissipation (Figures A4 -A6 in the Appendix A). In contrast, the S3 profile exhibits the opposite trend, with the wave heights increasing closer to land, suggesting wave shoaling influenced by bathymetry (Figures A4 -A6 in the Appendix A). This behavior is particularly evident between PT4 and PT3 in the S3 profile, especially under the 10 and 12 knots boat speed, where the super steep slope causes wave shoaling to occur rapidly over a very short distance (Figures A5-A6 in the Appendix A). The wave heights, in the S2 profile, initially decrease as the wave travels from PT3 to PT2, indicating partial energy loss or dispersion due to sparse vegetation (Figures A4 -A6 in the Appendix A). Moving further landward from PT2 to

PT1, in the S2 profile, the wave height increases, potentially due to depth-induced wave transformations (Figures A4 -A6 in the Appendix A).

After applying the filter to all water elevation time series obtained (see section 4.2.2), key wave parameters, including significant wave height (H_s), root mean square wave height (H_{rms}), and mean wave period (T_{mean}) were calculated. Among the three profiles, S1 consistently exhibits the lowest wave heights and periods, with H_s ranging from 0.01 to 0.09 m, and T_{mean} between 1.10 and 1.57 seconds (Table 2). Notably, the values of H_s remain nearly the same between 10 and 12 knots, suggesting limited variation in wave height at higher speeds within this profile (Table 2). In contrast, S2 shows the highest values in all wave parameters, with H_s reaching up to 0.18 m, and T_{mean} up to 2 seconds, particularly at higher velocities of 10-12 knots (Table 2). Profile S3 falls in between, with moderate wave heights and periods (Table 2).

Table 2. Computed wave parameters (H_s, H_{rms}, T_{mean}) across the three profiles and for the setup boat velocities; PTs – pressure transducers.

Profile	Boat velocity (knots)	PTs	H_s (m)	H_{rms} (m)	T_{mean} (seconds)
S1	12	PT5	0.09	0.07	1.42
		PT4	0.05	0.05	1.43
		PT3	0.04	0.04	1.40
		PT2	0.03	0.03	1.16
		PT1	0.04	0.03	1.18
	10	PT5	0.08	0.06	1.52
		PT4	0.05	0.04	1.52
		PT3	0.04	0.03	1.46
		PT2	0.03	0.02	1.36
		PT1	0.03	0.03	1.34
	8	PT5	0.04	0.03	1.57
		PT4	0.02	0.02	1.12
		PT3	0.01	0.01	1.16
		PT2	0.01	0.01	1.09
		PT1	0.02	0.01	1.10
S2	12	PT3	0.14	0.11	2.23
		PT2	0.13	0.10	1.89
		PT1	0.17	0.13	1.00
	10	PT3	0.18	0.13	2.06
		PT2	0.14	0.11	1.72
		PT1	0.14	0.11	1.40
	8	PT3	0.05	0.04	2.00
		PT2	0.04	0.03	1.44
		PT1	0.07	0.04	1.30
S3	12	PT4	0.12	0.10	2.34
		PT3	0.13	0.10	2.21
		PT2	0.13	0.11	2.20
		PT1	0.14	0.11	1.89
	10	PT4	0.15	0.11	2.20
		PT3	0.16	0.11	1.93
		PT2	0.16	0.11	1.92
		PT1	0.18	0.13	1.89
	8	PT4	0.09	0.06	1.65
		PT3	0.10	0.07	1.67
		PT2	0.10	0.07	1.75
		PT1	0.11	0.08	1.59

5.2.3. Wave attenuation quantification

Wave energy attenuation and shoaling vary significantly across profiles S1, S2 and S3 for boat speeds of 8, 10, and 12 knots (Figure 10). In the S1 profile, a consistent attenuation of wave energy is observed from PT5 to PT3 regardless of boat speed (Figure 10a). Further attenuation between PT3 and PT2 occurs only at 10 and 12 knots, while wave shoaling is evident from PT2 to PT1 only at 10 knots (Figure 10a). S2 profile also exhibits wave energy attenuation from PT3 to PT2 across all boat velocities, while shoaling between PT2 and PT1 is observed at 8 and 12 knots (Figure 10b). In contrast, the S3 profile shows consistent wave shoaling (wave energy increase) across the entire profile (Figure 10c).

In the S1 profile, wave energy is notably attenuated between PT5 and PT4, and again between PT4 and PT3 for all boat speeds, with the greatest attenuation at the lowest speed of 8 knots, approximately 55% between PT5 and PT4, and 75% between PT4 and PT3 (Figure 10a). At higher speeds of 10 and 12 knots, attenuation extends further landward, reaching approximately 44-56% between PT3 and PT2, with the lowest attenuation of about 36% occurring specifically between PT4 and PT3 at 12 knots (Figure 10a). Between the landward PTs (PT2 to PT1), there is a partial energy increase of 25% (shoaling) for the waves generated at 10 knots boat speed, which coincides with an increase in bottom slope, and therefore likely driven by wave transformation over a sudden slope gradient (Figure 10a). S2 profile displays minimal attenuation between PT3 and PT2, ranging from roughly 17% at 12 knots to 44% at 8 knots, and pronounced shoaling from PT2 to PT1, especially for 8 and 12 knots, aligning with a consistently rising slope landward (Figure 10b).

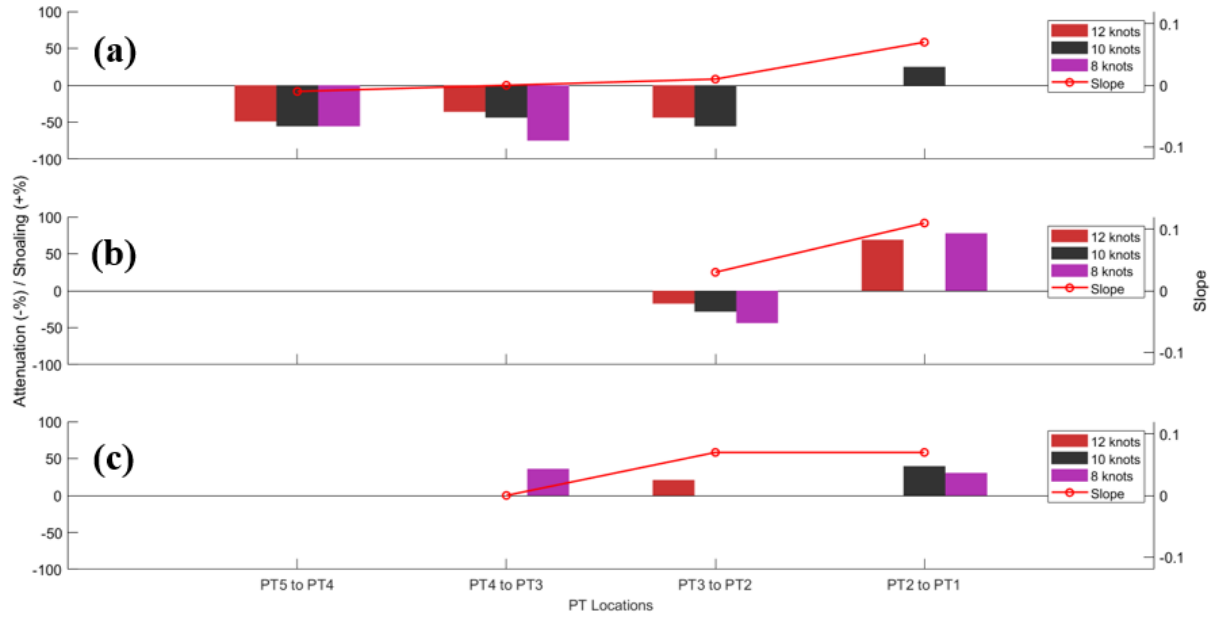

Figure 10. Measured wave energy attenuation (negative values; %) and shoaling (positive values; %), and slopes (red line) within consecutive PTs across (a) S1, (b) S2, and (c) S3 profiles, under boat velocity of 8 (magenta), 10 (black) and 12 (red) knots.

The wave attenuation coefficient (β) is highest at the lowest boat velocity and decreases as the speed increases (Figure 11). Specifically, at 8 knots, the coefficient is 0.024, indicating strong and rapid wave energy decay (Figure 11a). At 10 knots, the coefficient decreases to 0.017 (Figure 11b) and further drops to 0.015 at 12 knots (Figure 11c), representing the lowest attenuation rate among the three conditions. The latter suggests that waves generated at 8 knots travel the full length of the profile but with consistently lower wave heights and energy compared to waves generated at higher speeds. Waves generated at 12 knots maintain their energy over a longer distance, posing a potentially greater impact on shorelines. The uncertainty in wave attenuation coefficient (β) also decreases with increasing velocity; the larger uncertainty (0.08 in Figure 11a) at 8 knots reflects greater variability in experimental data or more influence from local disturbances, while the smaller uncertainty (0.03 in Figure 11c) at 12 knots indicates more stable and consistent wave behavior.

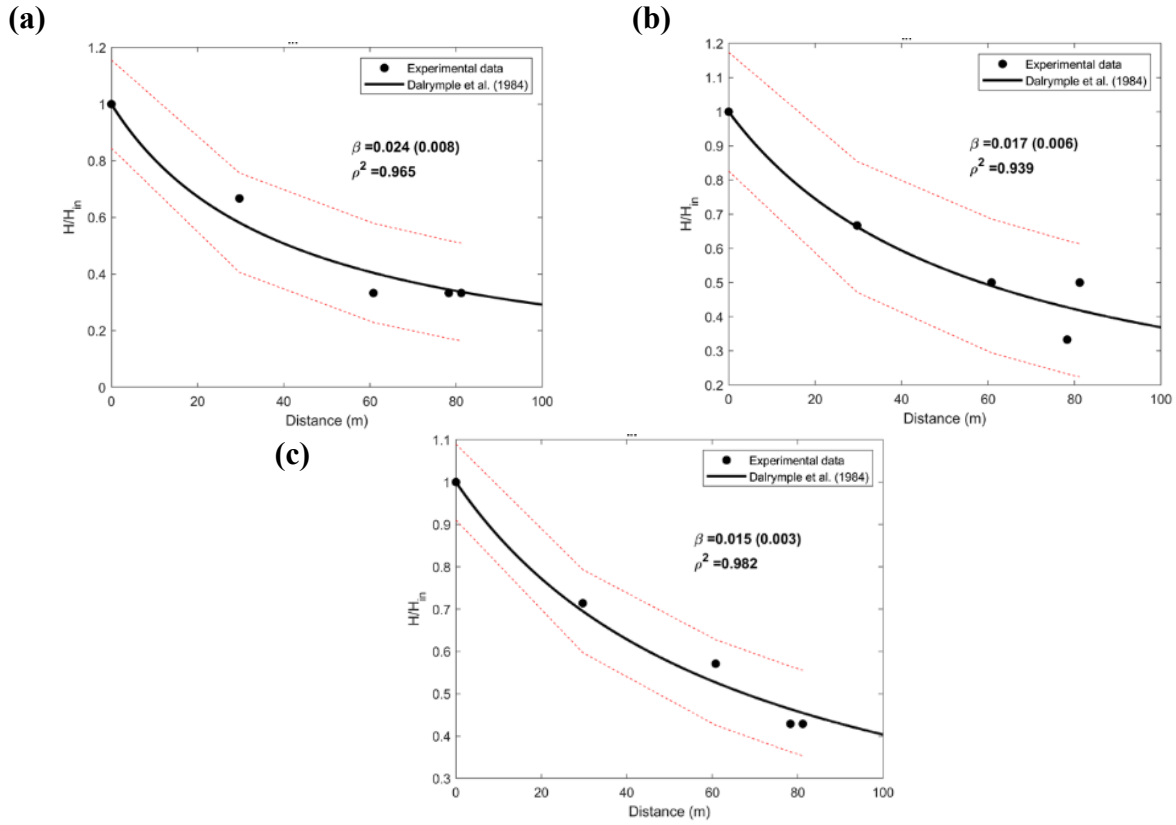

Figure 11. Wave height decay along S1 Profile for boat velocity of (a) 8, (b) 10 and (c) 12 knots. The solid black lines show the theoretical decay model from Dalrymple et al. (1984), while the black dots represent experimental data. The red dotted lines indicate the confidence bounds (uncertainty range) for the theoretical fit.

5.3. Mesh sensitivity test

In the S1 profile, both configurations show good agreement with in-situ measurements across all parameters (Figure 12a–d). The attenuation of H_s with distance is well captured by 105 cells/wavelength and similarly represented by 52 cells/wavelength, with both configurations successfully reproducing the general decay trend (Figure 12a). In the S2 profile, the performance gap between configurations becomes less pronounced, as 80, 40, and even 20 cells per wavelength align closely with measured H_s and transformation parameters across the profile

(Figure 12e–h). However, in the steeper and shorter profile S3, the importance of grid resolution becomes more evident. The 89 cells/wavelength accurately simulates the observed H_s, H_s/h, L/h, and H_s/L, while 55 cells/wavelength also performs reasonably well, maintaining close alignment with the measured data (Figure 12i–l). In contrast, 17 cells/wavelength exhibits noticeable discrepancies, particularly in the evolution of H_s (Figure 12i). Overall, the results from all three profiles consistently indicate that higher spatial resolution improves model accuracy. For the three profiles, a grid resolution ranging between 80 and 105 cells per wavelength is found to be the most reliable and is therefore selected for all subsequent SWAN simulations.

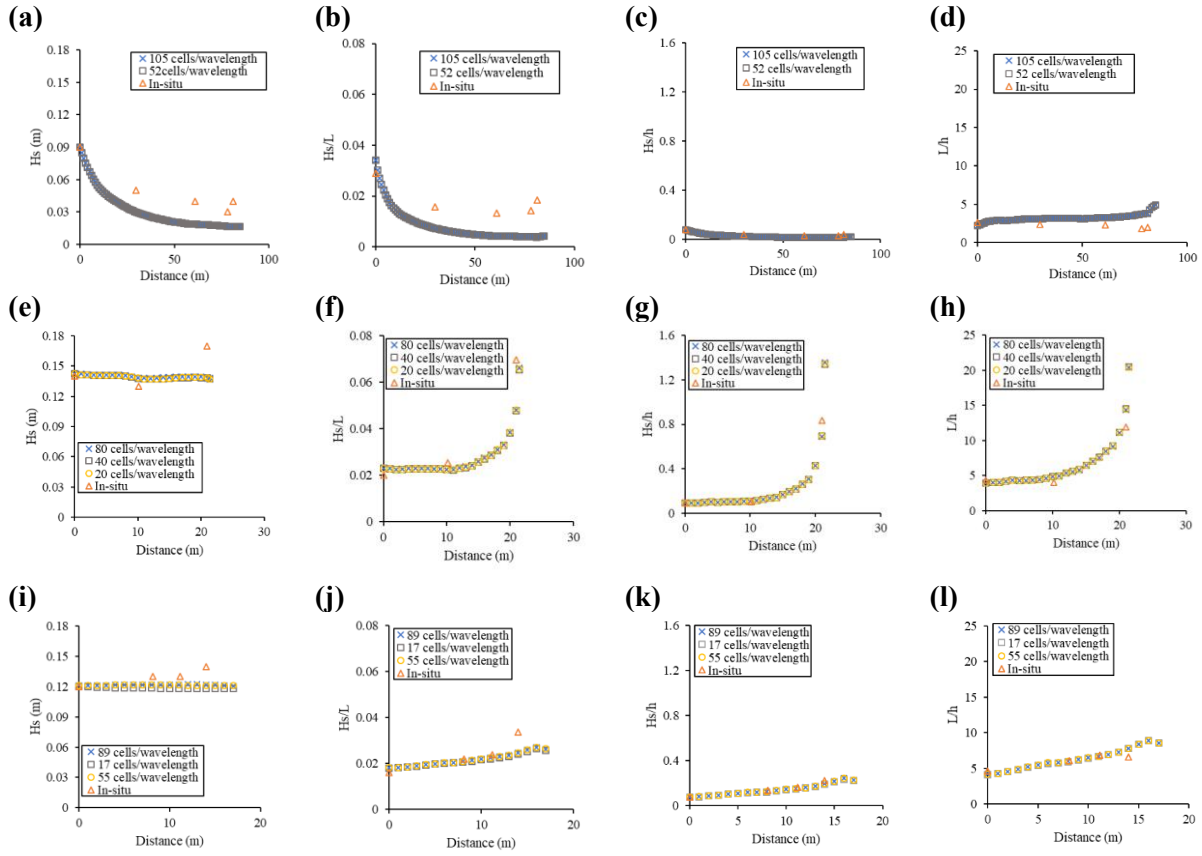

Figure 12. Sensitivity analysis in SWAN simulations for different grid resolutions, defined by the number of computational cells per wavelength, for a boat velocity of 12 knots, with simulated and measured wave parameters across profiles S1 (a–d), S2 (e–h), and S3 (i–l).

5.4. Model calibration

The model is calibrated using a combined vegetation parameter (N*) to represent vegetation effects, with *Zostera noltei* dominating the tidal flat (TF) and *Spartina maritima* dominating the low marsh (LM). N* is adjusted across all profiles to achieve good agreement between measured and simulated *Hs* at different boat velocities. It is evident that for both S1 and S2 profiles, TF dominated by *Zostera noltei* exhibits higher N* than LM dominated by *Spartina maritima*, primarily due to its higher vegetation density, as both species have almost negligible differences in height and stem diameter (Figure 13a-f). In the fully vegetated S1 profile, N* values are the highest compared to S2 and S3 profiles, indicating gradual wave attenuation along the profile and highlighting the role of vegetation in dissipating wave energy (Figure 13). At a boat speed of 8 knots, N* peaks at 18 (Figure 13a), indicating high wave energy dissipation, which corresponds to a higher drag coefficient (C_D) of 5.7 (see Table 3). For boat speeds of 10 and 12 knots, lower N* values (i.e., 7 for *Zostera noltei* and 4 for *Spartina maritima*) suggest reduced energy dissipation (Figure 13b-c), and therefore lower C_D values (2.2 for *Zostera noltei* and 0.84 for *Spartina maritima*) (Table 3). In the partially vegetated S2 profile, the model still captures wave attenuation trends well, with *Zostera noltei* represented by lowering N* values (N* = 5 to 2) followed by non-vegetated (N* = 0) LM (Figure 13d-f). Simulations using these N* values align more closely with field measurements at boat velocities of 8, 10 and 12 knots, emphasizing the damping effect of even sparse vegetation (Figure 13d-f). In the non-vegetated S3 profile (N* = 0), both measured and simulated H_s exhibit no attenuation (Figure 13g-i).

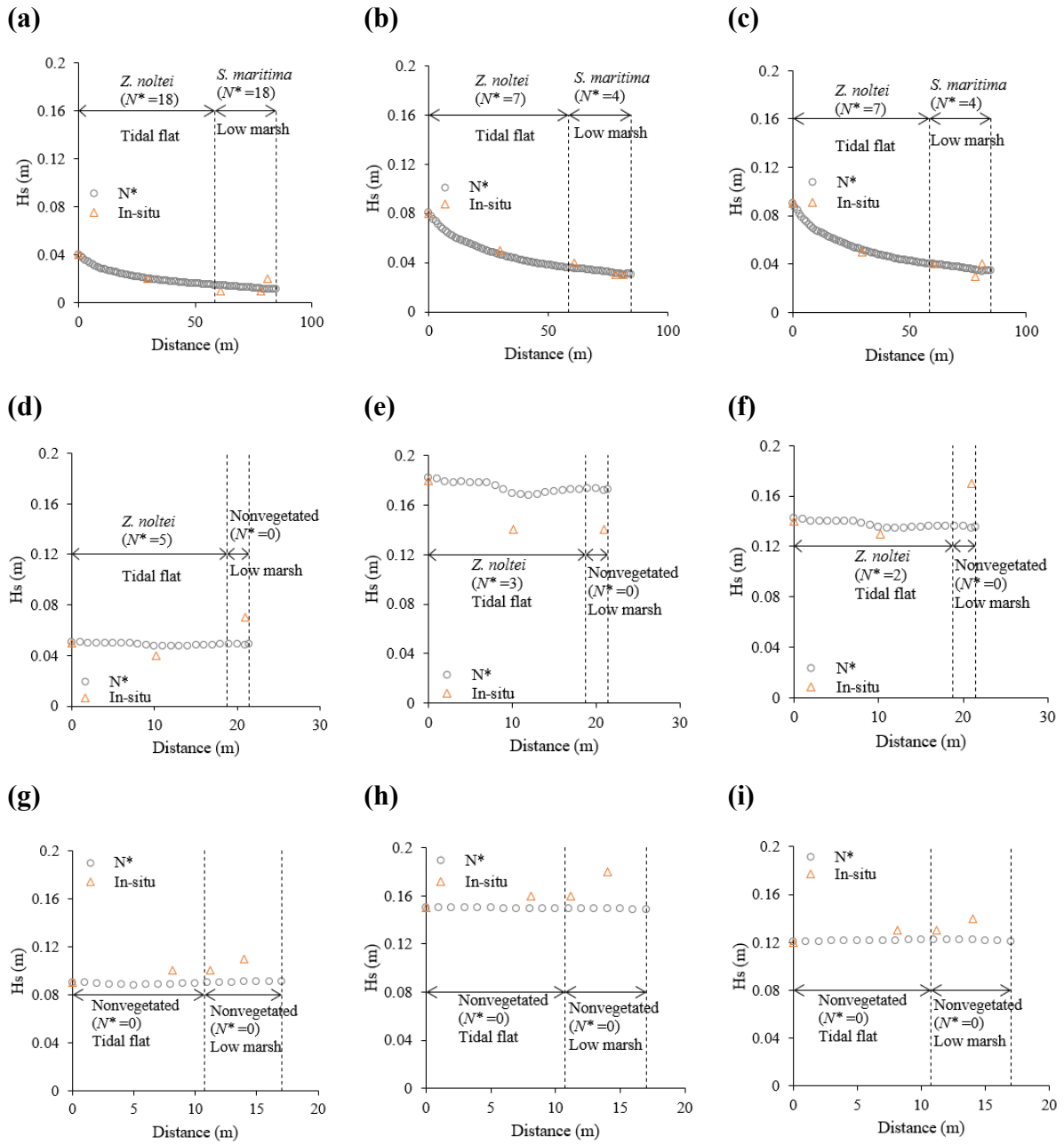

Figure 13. Model calibration for S1 (a–c), S2 (d–f), and S3 (g–i) profiles at boat velocity of 8 (1st column), 10 (2nd column) and 12 (3rd column) knots, comparing simulated (light black circle) and measured (yellow triangle) significant wave height (H_s).

5.5. C_D - KC relationship

The drag coefficients (C_D) for the S1 profile are calculated using Equation 5, based on the calibrated combined vegetation parameter (N*). This calculation incorporates in-situ measurements of vegetation height, stem diameter, and density for both *Zostera noltei* and *Spartina maritima* (see Table 3). The corresponding Keulegan–Carpenter (KC) numbers are derived using equation 6 (see section 4.3.4). As the S1 profile is fully vegetated, it provides a robust basis for examining the relationship between C_D and KC across different vegetation types. In S1, C_D decreases with increasing KC number for both species, with *Zostera noltei* exhibiting higher C_D values than *Spartina maritima* (Figure 14). *Zostera noltei*, which exhibits higher drag coefficient (C_D) at lower KC values (e.g., C_D = 5.7 at $KC \approx 20$ for 8 knots), consistently demonstrates greater resistance to flow compared to *Spartina maritima*, which shows slightly lower C_D values (e.g., C_D = 3.7 at $KC \approx 4$ for 8 knots) (Figure 14). At higher boat velocities (10 –12 knots), a reduced vegetation-induced drag is observed for both species. As wave height increases, leading to higher KC values, C_D continues to decrease, consistent with previous studies (Kelty et al., 2022; Lopez-Arias et al., 2024; Maza et al., 2019; Nepf, 2012; van Wesenbeeck et al., 2022) showing higher C_D at small KC and a reduced rate of change at larger KC values. In present study, similar C_D values are observed for the two largest KC values (Figure 14).

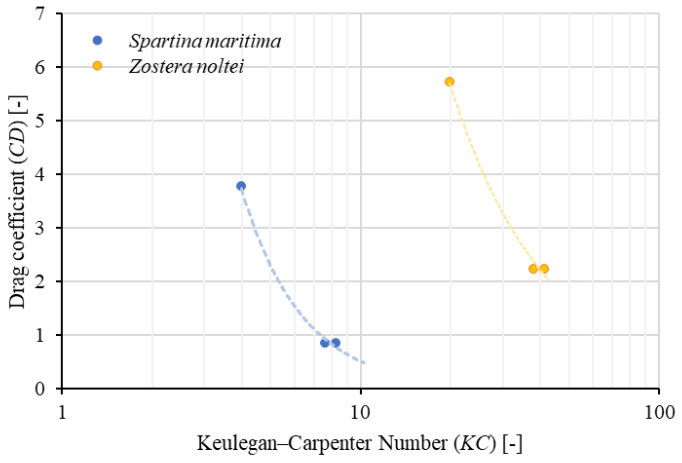

Figure 14. Relationship between drag coefficient (C_D) and Keulegan–Carpenter number (KC)

for *Zostera noltei* (yellow) and *Spartina maritima* (blue) in S1 profile.

Table 3. Calibrated combined vegetation parameter (N*) and corresponding drag coefficients (C_D) for *Zostera noltei* and *Spartina maritima* in S1 profile.

Species	Boat velocity (knots)	N*	C_D
Z. noltei	8	18	5.7
	10	7	2.2
	12		
S. maritima	8	18	3.7
	10	4	0.84
	12		

5.6. Modelling scenarios

Wave attenuation simulations are conducted across three scenarios to evaluate the effects of boat wakes variability (Scenario 1), vegetation density (Scenario 2), and profile geometry (Scenario 3). In scenario 1, the vegetation parameter N* ranges up to 18 for both *Zostera noltei* and *Spartina maritima* at lower wave heights, reflecting strong vegetation-induced drag (Table 4). Scenario 2 utilizes varied vegetation density between 1000 and 7000 stems/m^2, resulting in N* values between 1.5 and 10.2 for *Zostera noltei* and 1.2 to 6.9 for *Spartina maritima* (Table 4). Scenario 3 expands the analysis to all profiles (S1-S3), with N* values derive from C_D-KC relationships (see section 5.5) for the S1 profile. Based on model calibration, for the S2 profile (see section 5.4), N* ranges from zero in non-vegetated cases to 5 in sparse vegetated conditions, while the S3 profile simulates as non-vegetated based on field observation (Table 4).

Table 4. Summary of modelling scenarios and input parameters with calculated combined vegetation parameter (N^*) values for *Zostera noltei* and *Spartina maritima*.

	Category	Values					
Scenario 1	Topography	Profile S1					
	Water depth	1.1 meters					
	Wave characteristics (H_s, T_{mean}) and combined vegetation parameter (N^*)	H_s (m)	T_{mean} (s)	N^* for *Z. noltei*	N^* for *S. maritima*		
		0.04	1.5	18	18		
		0.08 0.15 0.22 0.41		7	4		
	Total simulations	1 profile × 5 wave characteristics and vegetation = 5					
Scenario 2	Topography	Profile S1					
	Water depth	1.1 meters					
	Wave characteristics (H_s, T_{mean}) and combined vegetation parameter (N^*)	Test cases	H_s (m)	T_{mean} (s)	Vegetation density (stems/m^2)		N^* for *Z. noltei*	N^* for *S. maritima*
					Z. noltei	*S. maritima*		
		N1	0.09	1.5	7000	2500	10.2	6.9
		N2			4800	1400	7	4
		N3			4000	2000	5.8	5.5
		N4			3000	1600	4.5	4.3
		N5			1000	2500	1.5	6.9
		N6			1000	450	1.5	1.2
	Total simulations	1 profile x 6 vegetation cases = 6						
Scenario 3	Topography	Depth profile between reference elevation E1 and E2 for profiles S1, S2 and S3 (Figure 9).						
	Water depth	1.1 meters						
	Profile, wave characteristics (H_s, T_{mean}) and combined vegetation parameter (N^*)		H_s (m)	T_{mean} (s)	N^* for *Z. noltei*	N^* for *S. maritima*	Case	
		S1	0.05	2	18	18	Reference	
			0.12 0.20		7	4		
			0.05 0.12 0.20		0	0	Non-vegetated	
		S2	0.05	2	5	0	Reference	
			0.12		3			
			0.20		2			
			0.05 0.12 0.20		0	0	Non-vegetated	
		S3	0.05 0.12 0.20	2	0	0	Reference (Non-vegetated based on field campaign)	
	Total simulations	(2 profiles × 3 wave characteristics × 2 cases) + 3 for S3 = 15						

5.6.1. Scenario 1: Potential attenuation of varying boat wakes using constant vegetation

It is depicted that wave attenuation increases (i.e., decreasing $H_{s,f}/H_{s,o}$) with increasing incoming wave height, for *Zostera noltei*, *Spartina maritima,* and the combination of both species (Figure 15). Among individual species, *Zostera noltei* consistently shows greater wave attenuation than *Spartina maritima*, particularly for higher incoming wave heights ($H_{s,o} \geq 0.15$ m) (Figure 15). For smaller incoming waves ($H_{s,o} = 0.04$ m and 0.08 m), the attenuation is almost similar between the two species, with *Spartina maritima* exhibiting slightly higher attenuation than *Zostera noltei* (Figure 15). This behaviour may be more strongly attributed to ecological differences between the vegetation zones, as field observations suggest that variations in mean water depth are minimal. The wave heights ($H_{s,o}$) of 0.04 m and 0.08 m exhibit similar attenuation across all vegetation types, with a 38% ($H_{s,f}/H_{s,o} = 0.62$) reduction observed for *Zostera noltei*, 40% ($H_{s,f}/H_{s,o} = 0.60$) for *Spartina maritima*, and 62% ($H_{s,f}/H_{s,o} = 0.38$) for the combined vegetation setup (Figure 15). The combined vegetation setup demonstrates the greatest attenuation across all wave conditions, highlighting this potential effect is enhanced when both species co-occur (Figure 15).

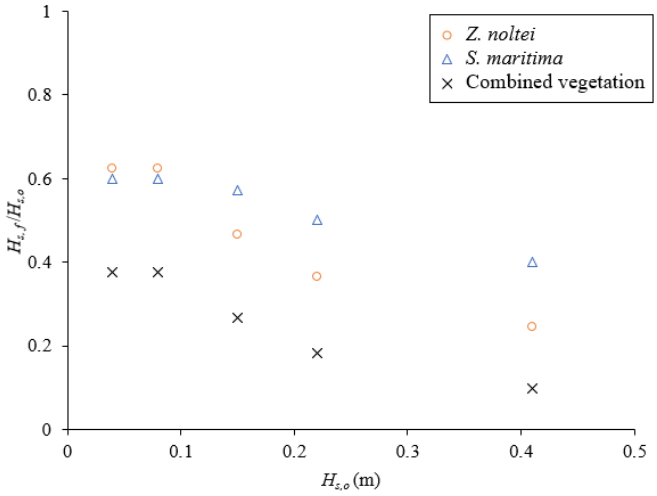

Figure 15. Variation of wave attenuation rate with incident wave height ($H_{s,o}$) for *Zostera noltei* (yellow circle), *Spartina maritima* (blue triangle), and combined vegetation (black cross mark).

5.6.2. Scenario 2: Influence of vegetation density on wave attenuation

The calculated combined vegetation parameter (N^*) decreases progressively with vegetation density decrease, from test case N1 to N6, for both *Zostera noltei* and *Spartina maritima*, with the exception in N5 (Table 4). In N5, despite the low density of *Zostera noltei* (1000 stems/m^2), *Spartina maritima* maintains a relatively high density of 2500 stems/m^2, resulting in a higher N* value for this species. Higher N^* indicates stronger vegetation-induced drag, which enhances wave energy dissipation (Nepf, 1999). As density decreases, wave attenuation capacity diminishes, which is reflected in increasing wave attenuation rate ($H_{s,f}/H_{s,o}$) from N1 to N6 (Figure 16). The greatest attenuation of approximately 68% occurs in N1, corresponding to the highest stem densities, 7000 stems/m^2 for *Zostera noltei* and 2500 stems/m^2 for *Spartina maritima* (Figure 16). A similar high attenuation is also observed in N2 with 4800 stems/m^2 for *Zostera noltei* and 1400 stems/m^2 for *Spartina maritima*, suggesting the saturation point beyond which further increases in density yield limited gains in wave damping (Figure 16). Finally, N6 with the lowest densities (1000 stems/m^2 for *Zostera noltei* and 450 stems/m^2 for *Spartina maritima*), shows the least attenuation (~22%), with $H_{s,f}/H_{s,o}$ approaching to 0.78 (Figure 16).

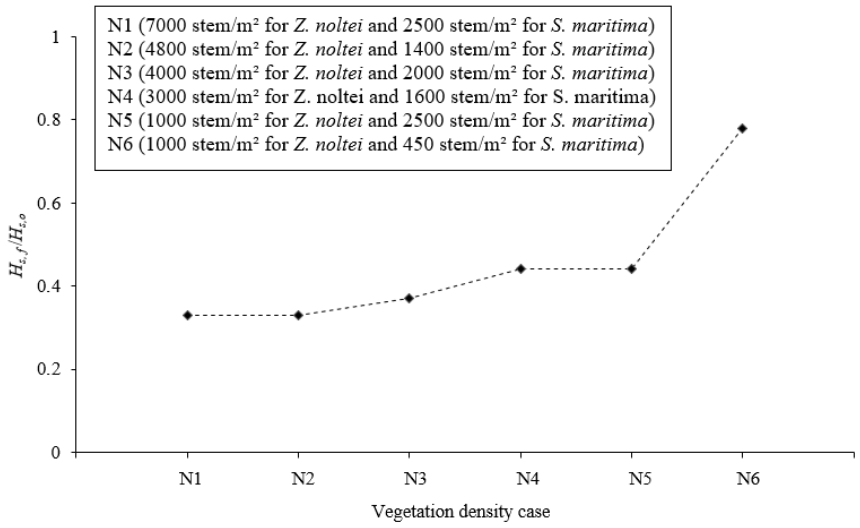

Figure 16. Wave attenuation rate ($H_{s,f}/H_{s,o}$) across varied vegetation density test cases (N1 - N6) for *Zostera noltei* and *Spartina maritima*.

5.6.3. Scenario 3: Influence of profile geometry on wave attenuation

Wave attenuation rates ($H_{s,f}/H_{s,o}$) are assessed for three distinct profiles (S1 - S3) under varying incident wave heights (0.05 m, 0.12 m, and 0.20 m). The analysis compares conditions with vegetation and profile geometry contributing to wave attenuation against a non-vegetated scenario, where only the profile geometry influences wave dissipation. In the reference conditions case, the S1 profile with dense vegetation cover exhibits the highest potential for wave energy dissipation, with $H_{s,f}/H_{s,o}$ consistently falling below 0.2 across all wave conditions, indicating around 85% reduction in wave energy due to the coupled effect of vegetation and profile geometry (Figure 17a). When vegetation is removed, the S1 profile shows only 5-10% attenuation ($H_{s,f}/H_{s,o} \geq 0.9$), highlighting the contribution of profile geometry alone (Figure 17a). In the shorter S2 profile with sparse vegetation, wave attenuation under reference conditions ranges from 6-10% ($H_{s,f}/H_{s,o}$ between 0.90 and 0.94), while the non-vegetated scenario shows minimal attenuation of only 0-2% ($H_{s,f}/H_{s,o}$ between 0.98 and 1) (Figure 17a). The shortest and non-vegetated S3 profile, displays no attenuation, confirming the minimal role of short, non-vegetated platforms in wave energy dissipation (Figure 17a). The difference in attenuation between reference and non-vegetated conditions reinforces the dominant role of vegetation, with vegetation alone contributing up to 75-80% of the overall attenuation in S1 (Figure 17b). In S2, the sparse vegetation accounts for just 4-10% of the overall attenuation (Figure 17b).

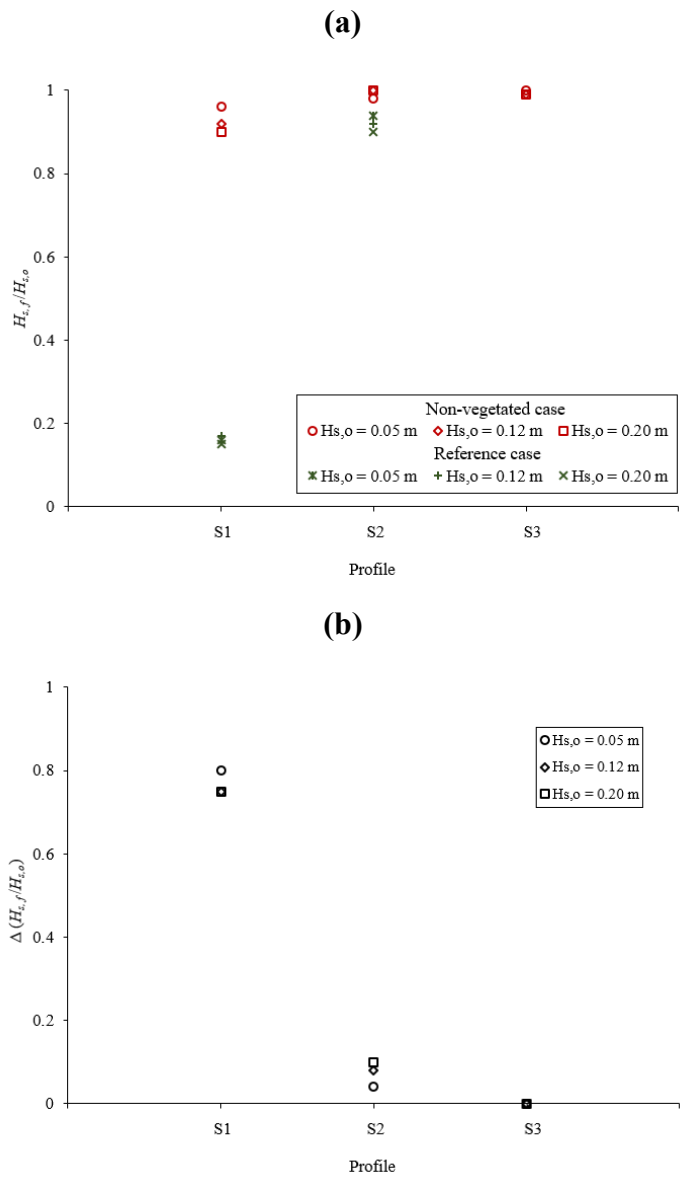

Figure 17. (a) Wave attenuation rate across profiles (S1 - S3) for reference (existing vegetation) and non-vegetated cases, and (b) difference in wave attenuation rate between reference and non-vegetated cases, under varying incident wave heights ($H_{s,o}$).

VI. Discussion

6.1. The role of profile geometry, vegetation type and vegetation density on wave attenuation

Based on the analysis of field data and modelling results, this study provides robust evidence that wave attenuation in coastal wetlands is governed by a complex interplay between vegetation species, shoots density, sediment properties, and topographic profile geometry. Previous studies have demonstrated the role of vegetation in reducing wave energy, often focusing on stem density or plant flexibility (Möller et al., 2014; Shepard et al., 2011; Wu and Cox, 2016; Zhang et al., 2022). However, there is a limited number of studies exploring the combined effects of these factors, particularly within the context of natural tidal wetlands. This study addresses that gap by comparing different vegetation arrangements and geometric configurations within a natural wetland to assess the wave attenuation potential of various ecomorphological combinations. Three distinct cross-shore profiles were selected for analysis, S1, S2 and S3.

This study allowed to quantify the potential wave attenuation attributable solely to platform geometry. The longest profile, S1, with approximately 100 meters in length and with a gentle slope, can reduce wave height by up to 10% (Figure 18). These findings align with Hewageegana et al. (2022) who used numerical modelling to test coastal marsh platform widths ranging from approximately 100 to 300 meters and slopes between 0.001 and 0.01, considering vegetation as constant, focusing primarily on the influence of marsh platform width and slope. They found that wider platforms with gentle slopes (around 0.001) achieved the highest water level attenuation by up to 30-40%, while narrower platforms (~100 meters) with steeper slopes (closer to 0.01) resulted in lower attenuation, typically 20-25%. Similarly, Stark et al. (2016) used numerical modelling which considered marsh widths ranging from 100 to 500 meters and elevations between 0.5 and 2 meters above mean sea level, assumed vegetation effects to be constant and showed that wider, elevated marsh platforms can reduce wave heights by 20-50%. In contrast, the present study focuses on platforms with lower elevations than those considered by Stark et al. (2016), which contributes to the relatively lower wave attenuation observed here. In the

shorter profile of around 20 meters, characterized by a steeper slope, exhibits wave attenuation nearly 2% (Figure 18). This means that even in the absence of vegetation, platform geometry alone can provide a measurable, though limited, degree of wave energy reduction. Although wave attenuation due to platform geometry alone is relatively low, it remains ecologically and functionally important, offering valuable guidance for the design of marsh restoration and management efforts.

Vegetation type plays a significant role in modulating wave-vegetation interactions and influencing the effectiveness of wave attenuation. The results of this study show that under low wave height ($H_{s,o}$) conditions, both *Zostera noltei* and *Spartina maritima* individually attenuate wave energy almost similarly (~40%), while their combination resulting in a slightly higher attenuation of 62% (Figure 18). Under high $H_{s,o}$, attenuation increases significantly, *Zostera noltei* achieves 75%, *Spartina maritima* 60%, and the combined vegetation reaches a maximum of 90% attenuation (Figure 18). This clearly illustrates a synergistic effect when both species are present, particularly under high $H_{s,o}$, where the interaction between vegetation structure and hydrodynamic forces becomes more pronounced. These findings are consistent with previous study by Ysebaert et al. (2011) conducted a field study in the Yangtze estuary and reported that *Spartina alterniflora* reduced wave heights by up to 80%. Moreover, Mazda et al. (1997) and Phan et al. (2019), which also observed that wave attenuation increases with rising wave heights, primarily due to intensified wave-vegetation interactions. Supporting evidence comes from Anderson and Smith (2014) who reported approximately 18-50% wave attenuation over a 9.8 m flume section for wave heights between 0.05 and 0.19 m using flexible, idealized vegetation mimicking generic salt marsh plants, and from Maza et al. (2019), who observed around 12-65% attenuation in a 1:6 scale physical model of a *Rhizophora* mangrove forest for wave heights from 0.05 to 0.20 m over a 26 meters forest. Additionally, the present results align with the work of Maza et al. (2022) who developed a generalized biomass-based framework using data from salt marsh species such as *Spartina maritima, Salicornia europaea, Halimione portulacoides and Juncus maritimus*, showing that combined standing biomass is a strong predictor of wave attenuation across various wave heights. Their numerical models indicate that typical salt marshes can attenuate wave heights by up to 60-80% for small to moderate waves (below ~0.2-

0.3 m). The enhanced attenuation observed in the mixed stands underscores the functional advantage of species diversity, suggesting that combined vegetation assemblages are more effective in dissipating wave energy than monocultures.

Vegetation density emerges as one of the prime factors influencing wave attenuation (Chen et al., 2007; Fonseca and Cahalan, 1992). The results of this study reinforce this finding, showing that increases in stem density significantly enhance energy dissipation. Under the low-density case (1000 stems/m^2 of *Zostera noltei* and 450 stems/m^2 of *Spartina maritima*), wave attenuation is limited to just about 22% (Figure 18). When the stem density of *Spartina maritima* alone is increased to 2500 stems/m^2, while *Zostera noltei* remains constant, attenuation increases by 34%, reaching 56% (Figure 18). However, in a combined high-density case (4800 stems/m^2 for *Zostera noltei* and 1400 stems/m^2 for *Spartina maritima*), attenuation further rises to 68%, confirming the importance of overall vegetation density (Figure 18). This aligns with the findings of Zhao et al. (2023), who emphasized that total vegetation density, rather than individual species contributions, plays a critical role in wave energy reduction across mixed salt marshes. Their study also found that reducing the coverage of *Spartina alterniflora* from 50% to 25%, led to a 43% decrease in wave attenuation capacity, highlighting the sensitivity of wave decay to decrease in vegetation density. Similarly, John et al. (2019) emphasized that maintaining dense vegetation is essential for optimal energy dissipation. Vuik et al. (2016), also documented wave attenuation ranging from 20% to 60% across vegetated marsh foreshores, depending on vegetation type and density. The present study identifies a saturation effect, since increasing vegetation density beyond 4800 stems/m^2 for *Zostera noltei* and 1400 stems/m^2 for *Spartina maritima* does not result in a further increase in wave attenuation (Figure 18), suggesting a threshold density beyond which additional planting yields minimal added benefit for wave attenuation. In particular, *Zostera noltei*, characterized by a high stem density and morphologically flexible structures, exerts greater hydrodynamic resistance compared to *Spartina maritima* (Figure 14). This higher resistance is not solely due to its higher drag coefficient (C_D), but results from the combined effect of C_D, stem density, and the vegetation's frontal area, all of which contribute to enhanced wave energy dissipation. This finding is supported by Schoutens et al. (2024), who conducted flume experiments using rope mimics of seven intertidal plant species (e.g., *Bolboschoenus*

maritimus, *Schoenoplectus tabernaemontani*, *Phragmites australis*, *Spartina anglica*, *Zostera noltei*, *Puccinellia maritima*, and *Elymus athericus*) common in north-west Europe. They observed that while wave attenuation increased with shoot density, the relationship followed a logarithmic trend, with diminishing returns beyond approximately 5000 shoots/m^2. Therefore, optimizing vegetation density rather than maximizing it indiscriminately, emerges as a practical and cost-effective strategy for the design and implementation of wetland nature-based solutions (NbS).

Furthermore, optimal vegetation density for effective wave attenuation depends strongly on sediment characteristics that support plant growth and establishment (Azevedo et al., 2016; Guerrero-Meseguer et al., 2021; Schwarz et al., 2015). Studies have shown that *Zostera noltei* thrives in fine, organic-rich sediments due to enhanced moisture retention and nutrient availability, which promote rhizome development and flowering (Azevedo et al., 2016; Guerrero-Meseguer et al., 2021). Similarly, salt marsh species like *Spartina alterniflora* benefit from ecomorphologic feedback between plant traits and fine cohesive sediments that stabilize the substrate and enable vegetation persistence (Schwarz et al., 2015). Similarly, the present study shows that different sediment types coincide with distinct vegetation patterns: the tidal flat (TF) supports dense vegetation (4800 stems/m^2 for *Zostera noltei*) in fine, silty, organic-rich sediments, while the lower marsh (LM) exhibits similarly dense stands (1400 stems/m^2 for *Spartina maritima*) in predominantly very fine sand (Figure 8). This suggests that high vegetation density can occur across contrasting sediment conditions, indicating that factors beyond sediment composition, such as species traits or hydrodynamic exposure, likely play a stronger role in determining plant distribution.

Collectively, these findings demonstrate that wave attenuation is maximized with dense vegetation in fine-grained, organic-rich sediments, and supported by a long, gentle sloping platform that align with previous studies emphasizing the importance of eco-morphological characteristics. For instance, Kadlec and Wallace (2008) highlighted how vegetation type, substrate composition, and spatial configuration govern the ecological performance of artificial wetlands, while Cheng et al. (2023) showed that sediment dynamics and landscape morphology

significantly influence the stability of tidal wetlands such as those in the Yangtze River Delta. These insights provide actionable guidance for coastal managers and restoration practitioners, effective NbS should integrate vegetation density, species traits, sediment characteristics, and platform geometry to enhance shoreline protection. Planning efforts should prioritize restoring or preserving high-density vegetation stands and gentle slopes while accounting for the ecological constraints imposed by site-specific sediment composition.

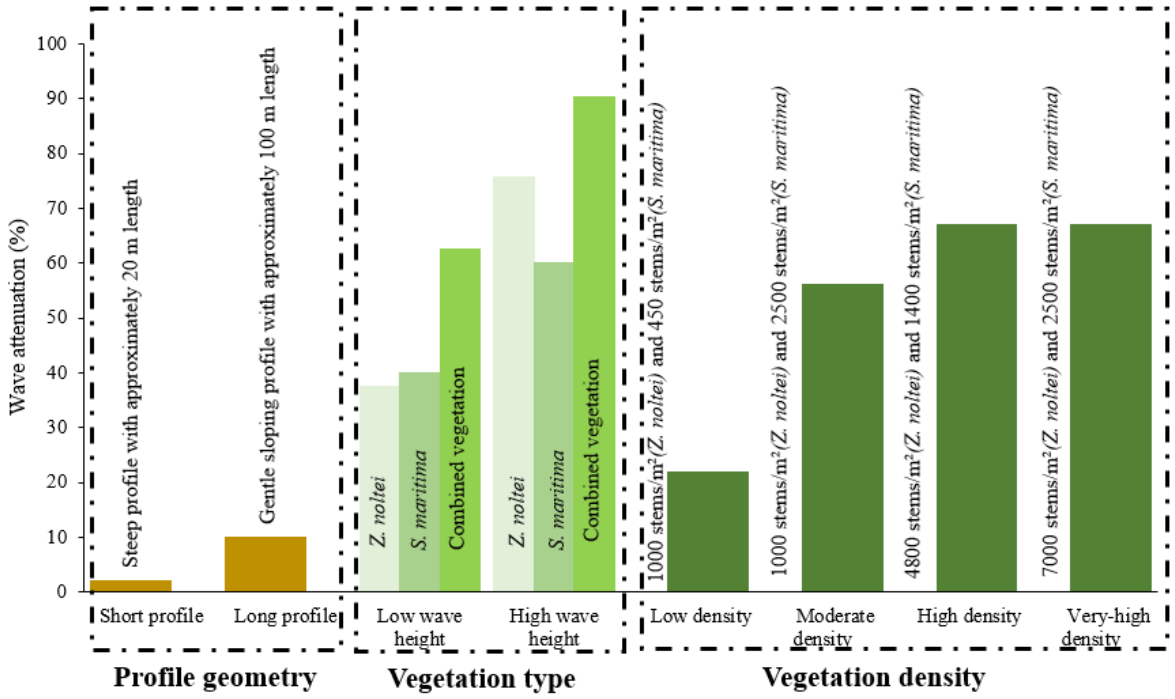

Figure 18. Conceptual diagram on wave attenuation by influence of profile geometry, vegetation type, and vegetation density.

6.2. Study limitation and future research

This study presents valuable insights into wave attenuation and wetland vegetation dynamics; however, several limitations might be acknowledged. Fieldwork was conducted at three profiles, providing spatial coverage but limiting the generalizability of findings across diverse marsh

conditions. The spatial resolution of Pressure Transducers (PTs) placement was restricted by site accessibility and vegetation distribution. Despite efforts to position PTs within homogeneous zones, small-scale heterogeneity in vegetation or sediment characteristics may not have been fully captured. Ecological and sediment sampling were limited to four locations per profile, which may not fully represent the existing spatial variability. Biomass estimation, based on 50 stems per quadrat (30 cm × 30 cm), is standard but may overlook dense vegetation structures. Additionally, hydrodynamic data were influenced by background noise from wind-generated waves and nearby vessel traffic, particularly ferries, which were eventually observed during the wave record analysis. Although filtering methods were applied to isolate boat wakes, some residual noise remained; however, its influence on the wave attenuation estimates is considered negligible. Due to site constraints within the natural park, it was not possible to test higher-energy waves, which would require either larger boats moving at higher speeds or the occurrence of wind storm induced waves, both of which were not feasible or predictable within the timeframe of the fieldwork. As a result, the study is primarily applicable to small waves, and further research is needed to assess wave attenuation under higher energetic conditions involving larger and longer waves.

The number of simulated scenarios of the present study was limited, focusing only on selected combinations of varying boat wakes, vegetation densities, and three distinct platform geometries. While this approach allowed for targeted analysis under controlled conditions, future research could expand on these findings by exploring additional geometric configurations to further understand the variability in wave attenuation. Furthermore, tides affect water depth, wave energy, and vegetation submergence, all of which significantly influence wave attenuation capacity (Möller et al., 2014). This study analyzed wave attenuation under high tide conditions, during which wave activity is most relevant, as wave propagation is minimal or absent during low tide. Future studies should consider a broader range of tidal conditions, particularly larger tidal ranges and higher water levels, to further explore their influence on wave attenuation.

To improve the generalizability and robustness of the findings, future research should integrate both comprehensive field measurements and expanded modeling scenarios across a broader

range of ecological settings, plant species, and wave conditions. Specifically, it is recommended to include a greater variety of marsh platform geometries, encompassing different shapes, sizes, and slopes, to better represent the morphological diversity of natural marshes. Additional profiles should be tested to capture spatial variability, and a higher number of pressure transducers (PTs) should be deployed along the transects to enhance the resolution of hydrodynamic measurements. Furthermore, increasing the sampling density for both ecological and sedimentary parameters would allow for a more detailed understanding of how vegetation structure and sediment characteristics influence wave attenuation processes. Together, these efforts would contribute to optimizing marsh design for both coastal protection and ecological functionality.

VII. Conclusion

Nature-based solutions (NbS) based on salt marshes restoration, provide sustainable and cost-effective coastal protection by reducing wave energy and mitigating flood risks, particularly in the context of climate change. While their role in attenuating wind-generated waves is well established, their capacity to reduce energy from boat wakes remains less understood. This study addresses the existing research gap by evaluating the effectiveness of wetlands vegetation in dissipating random wave energy, particularly from boat wakes, through a combination of field measurements and SWAN model simulations. By exploring the influence of varied boat wakes, vegetation density, and profile geometry, this study aims to support future restoration efforts and inform nature-based coastal protection strategies.

The results of this study demonstrate that wave attenuation is strongly influenced by the interaction of vegetation density and profile geometry. The densely vegetated profile achieved substantial wave energy reduction, while sparse or non-vegetated profiles exhibited minimal wave attenuation, highlighting the critical role of vegetation. Among vegetation types, *Zostera noltei* consistently provides greater attenuation than *Spartina maritima* for larger wave heights ($H_{s,o} \geq 0.15$ m), though mixed-species vegetation offers the most effective natural buffer. Wave attenuation increases with the increase of $H_{s,o}$ for both species and combined vegetation case. Additionally, higher vegetation densities significantly enhance wave dissipation, with up to 68% attenuation observed at high stem densities, whereas low-density stands showed limited wave energy reduction. The study also identifies a saturation density at approximately 4800 stems/m^2 for *Zostera noltei* and 1400 stems/m^2 for *Spartina maritima*, beyond which further increases in vegetation density do not significantly enhance wave attenuation. Although with less prominence, profile geometry also contributed to attenuation, with longer (~100 m), gently sloping profile reducing wave energy by approximately 10% of the overall attenuation, while shorter (~20 m), steeper profile was notably less effective. Collectively, these findings emphasize that effective wave energy reduction in coastal environments requires the synergistic combination of dense vegetation and favorable platform geometry, key considerations for

advancing nature-based coastal protection.

This study is limited by the use of only three monitoring profiles, restricted spatial sampling resolution, and small boat wakes, which may not fully capture the complexity of wave-vegetation interactions and spatial variability in natural wetlands. Future studies should combine comprehensive field measurements and expanded modeling across diverse ecological settings, incorporating tidal dynamics and varied marsh geometry and vegetation arrangements to optimize wave attenuation and ecological benefits. It is also important to test the attenuation capabilities of other salt marsh species to boat wakes.

The results of this study offer valuable guidance for coastal managers aiming to implement effective and sustainable wetland nature-based solutions. Prioritizing the preservation and restoration of dense, mixed-species vegetated habitats, which exhibit strong wave attenuation, is crucial for enhancing natural coastal defense. Incorporating longer, gently sloping profiles with dense vegetation can significantly enhance wave energy dissipation, reducing the need for expensive engineered structures. Additionally, understanding how wave attenuation varies with boat wakes enables the design of adaptive, site-specific management strategies that maximize the protective functions of coastal wetlands. These insights empower coastal managers to design resilient, cost-effective, and ecologically sound measures to reduce marsh edge erosion, and adapt to the challenges posed by sea-level rise and climate change.

In conclusion, this study underscores the vital role of integrating vegetation density, species composition, and marsh platform geometry in designing effective nature-based coastal protection. By addressing the complexities of wave-vegetation interactions and recognizing the influence of boat wakes, future restoration and management efforts can be better tailored to sustain and enhance the multifunctional benefits of coastal wetlands

References

Anderson, M. E., & Smith, J. (2014). Wave attenuation by flexible, idealized salt marsh vegetation. *Coastal Engineering, 83*, 82-92.

Augustin, L. N., Irish, J. L., & Lynett, P. (2009). Laboratory and numerical studies of wave damping by emergent and near-emergent wetland vegetation. *Coastal Engineering, 56*(3), 332-340.

Azevedo, A., Dias, J. M., & Lillebø, A. I. (2016). Thriving of Zostera noltei under intertidal conditions: implications for the modelling of seagrass populations. *Marine Biology, 163*, 1-8.

Barman, A., Rajak, F., & Jha, R. (2024). Integrating Wetlands as Nature-Based Solutions for Sustainable Built Environments: A Comprehensive Review. *Engineering, Technology & Applied Science Research, 14*(6), 18670-18680.

Bilkovic, D., M. Mitchell, J. Davis, E. Andrews, A. King, P. Mason, J. Herman, N. Tahvildari, J. Davis. (2017). Review of boat wake wave impacts on shoreline erosion and potential solutions for the Chesapeake Bay. *STAC Publication Number 17-002, Edgewater, MD*, 68 pp.

Bilkovic, D. M., Mitchell, M. M., Davis, J., Herman, J., Andrews, E., King, A., . . . Dixon, R. L. (2019). Defining boat wake impacts on shoreline stability toward management and policy solutions. *Ocean & Coastal Management, 182*, 104945.

Blott, S. J., & Pye, K. (2001). GRADISTAT: a grain size distribution and statistics package for the analysis of unconsolidated sediments. *Earth surface processes and Landforms, 26*(11), 1237-1248.

Blott, S. J., & Pye, K. (2012). Particle size scales and classification of sediment types based on particle size distributions: Review and recommended procedures. *Sedimentology, 59*(7), 2071-2096.

Booij, N., Ris, R. C., & Holthuijsen, L. H. (1999). A third-generation wave model for coastal regions: 1. Model description and validation. *Journal of Geophysical Research: Oceans, 104*(C4), 7649-7666.

Bradley, K., & Houser, C. (2009). Relative velocity of seagrass blades: Implications for wave attenuation in low-energy environments. *Journal of Geophysical Research: Earth Surface, 114*(F1).

Cabaço, S., Machas, R., & Santos, R. (2009). Individual and population plasticity of the seagrass Zostera noltii along a vertical intertidal gradient. *Estuarine, Coastal and Shelf Science, 82*(2), 301-308.

Carrasco, A. R., Plomaritis, T., Reyns, J., Ferreira, Ó., & Roelvink, D. (2018). Tide circulation patterns in a coastal lagoon under sea-level rise. *Ocean Dynamics, 68*, 1121-1139.

Castagno, K. A., Tomiczek, T., Shepard, C. C., Beck, M. W., Bowden, A. A., O'Donnell, K., & Scyphers, S. B. (2021). Resistance, resilience, and recovery of salt marshes in the Florida Panhandle following Hurricane Michael. *Scientific Reports, 11*(1), 20381.

Castellanos, E., Heredia, C., Figueroa, M., & Davy, A. (1998). Tiller dynamics of Spartina maritima in successional and non-successional Mediterranean salt marsh. *Plant Ecology, 137*, 213-225.

Chapman, V. J. (2016). *Coastal vegetation*: Elsevier.

Chen, S.-N., Sanford, L. P., Koch, E. W., Shi, F., & North, E. W. (2007). A nearshore model to investigate the effects of seagrass bed geometry on wave attenuation and suspended sediment transport. *Estuaries and Coasts, 30*, 296-310.

Cheng, S., Zeng, X., Wang, Z., Zeng, C., & Cao, L. (2023). Spatiotemporal variations of tidal flat landscape patterns and driving forces in the Yangtze River Delta, China. *Frontiers in Marine Science, 9*, 1086775.

Costanza, R., Pérez-Maqueo, O., Martinez, M. L., Sutton, P., Anderson, S. J., & Mulder, K. (2008). The value of coastal wetlands for hurricane protection. *Ambio*, 241-248.

Dalrymple, R. A., Kirby, J. T., & Hwang, P. A. (1984). Wave diffraction due to areas of energy dissipation. *Journal of waterway, port, coastal, and ocean engineering, 110*(1), 67-79.

Ferreira, Ó., Matias, A., & Pacheco, A. (2016). The east coast of Algarve: a barrier island dominated coast. *Thalassas: An International Journal of Marine Sciences, 32*, 75-85.

Fonseca, M. S., & Cahalan, J. A. (1992). A preliminary evaluation of wave attenuation by four species of seagrass. *Estuarine, Coastal and Shelf Science, 35*(6), 565-576.

Gedan, K. B., Kirwan, M. L., Wolanski, E., Barbier, E. B., & Silliman, B. R. (2011). The present

and future role of coastal wetland vegetation in protecting shorelines: answering recent challenges to the paradigm. *Climatic change, 106*, 7-29.

Glenn-Lewin, D. (1992). Plant Succession: Theory and Prediction. In: Chapman and Hall.

Grizzle, R. E., Short, F. T., Newell, C. R., Hoven, H., & Kindblom, L. (1996). Hydrodynamically induced synchronous waving of seagrasses:'monami'and its possible effects on larval mussel settlement. *Journal of Experimental Marine Biology and Ecology, 206*(1-2), 165-177.

Guerrero-Meseguer, L., Veiga, P., Sampaio, L., & Rubal, M. (2021). Sediment characteristics determine the flowering effort of Zostera noltei meadows inhabiting a human-dominated lagoon. *Plants, 10*(7), 1387.

Hewageegana, V., Bilskie, M., Woodson, C., & Bledsoe, B. (2022). The effects of coastal marsh geometry and surge scales on water level attenuation. *Ecological Engineering, 185*, 106813.

Howard, J., Hoyt, S., Isensee, K., Telszewski, M., & Pidgeon, E. (2014). Coastal blue carbon: methods for assessing carbon stocks and emissions factors in mangroves, tidal salt marshes, and seagrasses.

Irish, J. L., Augustin, L., Balsmeirer, G., & Kaihatu, J. M. (2008). Wave dynamics in coastal wetlands: a state-of-knowledge review with emphasis on wetland functionality for storm damage reduction. *Shore and Beach, 76*, 52-56.

IUCN. (2016). Nature-based Solutions to address societal challenges. Gland, Switzerland: International Union for Conservation of Nature.

John, B. M., Shirlal, K. G., & Rao, S. (2019). Laboratory investigations of wave attenuation by simulated vegetation of varying densities. *ISH Journal of Hydraulic Engineering, 25*(2), 203-213.

Kadlec, R. H., & Wallace, S. (2008). *Treatment wetlands*: CRC press.

Kelty, K., Tomiczek, T., Cox, D. T., Lomonaco, P., & Mitchell, W. (2022). Prototype-scale physical model of wave attenuation through a mangrove forest of moderate cross-shore thickness: Lidar-based characterization and Reynolds scaling for engineering with nature. *Frontiers in Marine Science, 8*, 780946.

Kumar, M., Boski, T., González-Vila, F. J., de la Rosa, J. M., & González-Pérez, J. A. (2020).

Discerning natural and anthropogenic organic matter inputs to salt marsh sediments of Ria Formosa lagoon (South Portugal). *Environmental Science and Pollution Research, 27*, 28962-28985.

Lopez-Arias, F., Maza, M., Calleja, F., Govaere, G., & Lara, J. L. (2024). Integrated drag coefficient formula for estimating the wave attenuation capacity of Rhizophora sp. mangrove forests. *Frontiers in Marine Science, 11*, 1383368.

Magdalena, I., Andadari, G. R., & Reeve, D. E. (2022). An integrated study of wave attenuation by vegetation. *Wave Motion, 110*, 102878.

Maza, M., Lara, J. L., & Losada, I. J. (2019). Experimental analysis of wave attenuation and drag forces in a realistic fringe Rhizophora mangrove forest. *Advances in Water Resources, 131*, 103376.

Maza, M., Lara, J. L., & Losada, I. J. (2022). A paradigm shift in the quantification of wave energy attenuation due to saltmarshes based on their standing biomass. *Scientific Reports, 12*(1), 13883.

Mazda, Y., Magi, M., Kogo, M., & Hong, P. N. (1997). Mangroves as a coastal protection from waves in the Tong King delta, Vietnam. *Mangroves and Salt marshes, 1*, 127-135.

Mcleod, E., Chmura, G. L., Bouillon, S., Salm, R., Björk, M., Duarte, C. M., . . . Silliman, B. R. (2011). A blueprint for blue carbon: toward an improved understanding of the role of vegetated coastal habitats in sequestering CO2. *Frontiers in Ecology and the Environment, 9*(10), 552-560.

Mendez, F. J., & Losada, I. J. (2004). An empirical model to estimate the propagation of random breaking and nonbreaking waves over vegetation fields. *Coastal Engineering, 51*(2), 103-118.

Méndez, F. J., Losada, I. J., & Losada, M. A. (1999). Hydrodynamics induced by wind waves in a vegetation field. *Journal of Geophysical Research: Oceans, 104*(C8), 18383-18396.

Mitsch, W. J., & Gosselink, J. G. (2015). *Wetlands*: John wiley & sons.

Möller, I., Kudella, M., Rupprecht, F., Spencer, T., Paul, M., Van Wesenbeeck, B. K., . . . Miranda-Lange, M. (2014). Wave attenuation over coastal salt marshes under storm surge conditions. *Nature Geoscience, 7*(10), 727-731.

Möller, I., & Spencer, T. (2002). Wave dissipation over macro-tidal saltmarshes: Effects of marsh

edge typology and vegetation change. *Journal of Coastal Research*(36), 506-521.

Nepf, H., & Ghisalberti, M. (2008). Flow and transport in channels with submerged vegetation. *Acta Geophysica, 56*, 753-777.

Nepf, H. M. (1999). Drag, turbulence, and diffusion in flow through emergent vegetation. *Water resources research, 35*(2), 479-489.

Nepf, H. M. (2012). Flow and transport in regions with aquatic vegetation. *Annual review of fluid mechanics, 44*(1), 123-142.

Newton, A., Cañedo-Argüelles, M., March, D., Goela, P., Cristina, S., Zacarias, M., & Icely, J. (2022). Assessing the effectiveness of management measures in the Ria Formosa coastal lagoon, Portugal. *Frontiers in Ecology and Evolution, 10*, 508218.

Ondiviela, B., Fernández, L., Puente, A., García-Castrillo, G., & Juanes, J. A. (2018). Characterization of a resilient seagrass meadow during a decline period. *Sci. Mar, 82*, 67-75.

Pacheco, A., Ferreira, Ó., Williams, J., Garel, E., Vila-Concejo, A., & Dias, J. (2010). Hydrodynamics and equilibrium of a multiple-inlet system. *Marine Geology, 274*(1-4), 32-42.

Passaro, M., Hemer, M. A., Quartly, G. D., Schwatke, C., Dettmering, D., & Seitz, F. (2021). Global coastal attenuation of wind-waves observed with radar altimetry. *Nature Communications, 12*(1), 3812.

Paul, M., & Amos, C. (2011). Spatial and seasonal variation in wave attenuation over Zostera noltii. *Journal of Geophysical Research: Oceans, 116*(C8).

Phan, K., Stive, M., Zijlema, M., Truong, H., & Aarninkhof, S. (2019). The effects of wave non-linearity on wave attenuation by vegetation. *Coastal Engineering, 147*, 63-74.

Reguero, B. G., Beck, M. W., Schmid, D., Stadtmüller, D., Raepple, J., Schüssele, S., & Pfliegner, K. (2020). Financing coastal resilience by combining nature-based risk reduction with insurance. *Ecological Economics, 169*, 106487.

Reid, W. V., Mooney, H. A., Cropper, A., Capistrano, D., Carpenter, S. R., Chopra, K., . . . Hassan, R. (2005). *Ecosystems and human well-being-Synthesis: A report of the Millennium Ecosystem Assessment*: Island Press.

Salles, P. (2001). Hydrodynamic controls on multiple tidal inlet persistence. . *PhD Thesis,*

Massachusetts Institute of Technology and Woods Hole. Oceanographic Institution, Woods Hole, USA.

Sánchez, J. M., Otero, X. L., Izco, J., & Macías, F. (1997). Growth form and population density of Spartina maritima (Curtis) Fernald in Northwest Spain. *Wetlands, 17*, 368-374.

Santos, R., Duque-Núñez, N., de Los Santos, C. B., Martins, M., Carrasco, A. R., & Veiga-Pires, C. (2019). Superficial sedimentary stocks and sources of carbon and nitrogen in coastal vegetated assemblages along a flow gradient. *Scientific Reports, 9*(1), 610.

Schoutens, K., Silinski, A., Belliard, J. P., Bouma, T. J., Temmerman, S., & Schoelynck, J. (2024). Wave attenuation by intertidal vegetation is mediated by trade-offs between shoot-and canopy-scale plant traits. *Journal of Applied Ecology, 61*(11), 2628-2637.

Schwarz, C., Bouma, T., Zhang, L., Temmerman, S., Ysebaert, T., & Herman, P. (2015). Interactions between plant traits and sediment characteristics influencing species establishment and scale-dependent feedbacks in salt marsh ecosystems. *Geomorphology, 250*, 298-307.

Shepard, C. C., Crain, C. M., & Beck, M. W. (2011). The protective role of coastal marshes: a systematic review and meta-analysis. *PloS one, 6*(11), e27374.

Silvestri, S. (2005). Tidal regime, salinity and salt marsh plant zonation. *Estuarine, Coastal and Shelf Science, 62*(1-2), 119-130.

Siverd, C. G., Hagen, S. C., Bilskie, M. V., Braud, D. H., & Twilley, R. R. (2020). Quantifying storm surge and risk reduction costs: a case study for Lafitte, Louisiana. *Climatic change, 161*, 201-223.

Smolders, S., Plancke, Y., Ides, S., Meire, P., & Temmerman, S. (2015). Role of intertidal wetlands for tidal and storm tide attenuation along a confined estuary: a model study. *Natural Hazards and Earth System Sciences, 15*(7), 1659-1675.

Stark, J., Plancke, Y., Ides, S., Meire, P., & Temmerman, S. (2016). Coastal flood protection by a combined nature-based and engineering approach: Modeling the effects of marsh geometry and surrounding dikes. *Estuarine, Coastal and Shelf Science, 175*, 34-45.

Suzuki, T., Zijlema, M., Burger, B., Meijer, M. C., & Narayan, S. (2012). Wave dissipation by vegetation with layer schematization in SWAN. *Coastal Engineering, 59*(1), 64-71.

Taramelli, A., Valentini, E., Piedelobo, L., Righini, M., & Cappucci, S. (2021). Assessment of

State Transition Dynamics of Coastal Wetlands in Northern Venice Lagoon, Italy. *Sustainability, 13*(8), 4102.

Thorslund, J., Jarsjo, J., Jaramillo, F., Jawitz, J. W., Manzoni, S., Basu, N. B., . . . Goldenberg, R. (2017). Wetlands as large-scale nature-based solutions: Status and challenges for research, engineering and management. *Ecological Engineering, 108*, 489-497.

Tucker, M. J., & Pitt, E. G. (2001). *Waves in ocean engineering*.

van Wesenbeeck, B. K., Wolters, G., Antolínez, J. A., Kalloe, S. A., Hofland, B., de Boer, W. P., . . . Bouma, T. J. (2022). Wave attenuation through forests under extreme conditions. *Scientific Reports, 12*(1), 1884.

van Zelst, V. T., Dijkstra, J. T., van Wesenbeeck, B. K., Eilander, D., Morris, E. P., Winsemius, H. C., . . . de Vries, M. B. (2021). Cutting the costs of coastal protection by integrating vegetation in flood defences. *Nature Communications, 12*(1), 6533.

Vuik, V., Jonkman, S. N., Borsje, B. W., & Suzuki, T. (2016). Nature-based flood protection: The efficiency of vegetated foreshores for reducing wave loads on coastal dikes. *Coastal Engineering, 116*, 42-56.

Wu, W.-C., & Cox, D. T. (2016). Effects of vertical variation in vegetation density on wave attenuation. *Journal of waterway, port, coastal, and ocean engineering, 142*(2), 04015020.

Ysebaert, T., Yang, S.-L., Zhang, L., He, Q., Bouma, T. J., & Herman, P. M. (2011). Wave attenuation by two contrasting ecosystem engineering salt marsh macrophytes in the intertidal pioneer zone. *Wetlands, 31*, 1043-1054.

Zhang, W., Ge, Z.-M., Li, S.-H., Tan, L.-S., Zhou, K., Li, Y.-L., . . . Dai, Z.-J. (2022). The role of seasonal vegetation properties in determining the wave attenuation capacity of coastal marshes: Implications for building natural defenses. *Ecological Engineering, 175*, 106494.

Zhao, Y., Peng, Z., He, Q., & Ma, Y. (2023). Wave attenuation over combined salt marsh vegetation. *Ocean engineering, 267*, 113234.

Appendix A

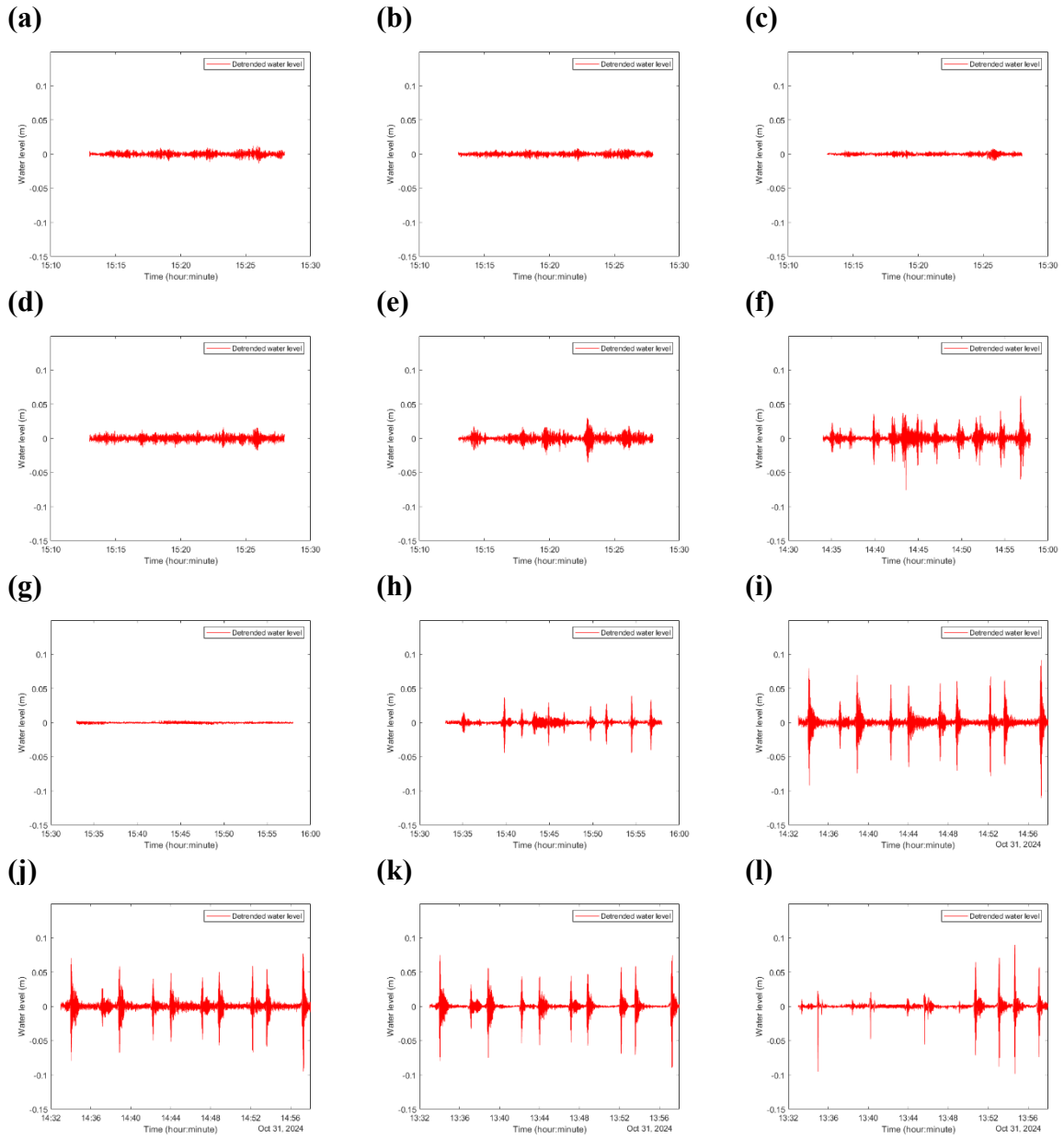

Figure A1. Water level variations over time after tidal signal removal for the S1 profile (PT1–PT5, panels a–e), S2 profile (PT1–PT3, panels f–h), and S3 profile (PT1–PT4, panels i–l), for boat velocity of 8 knots.

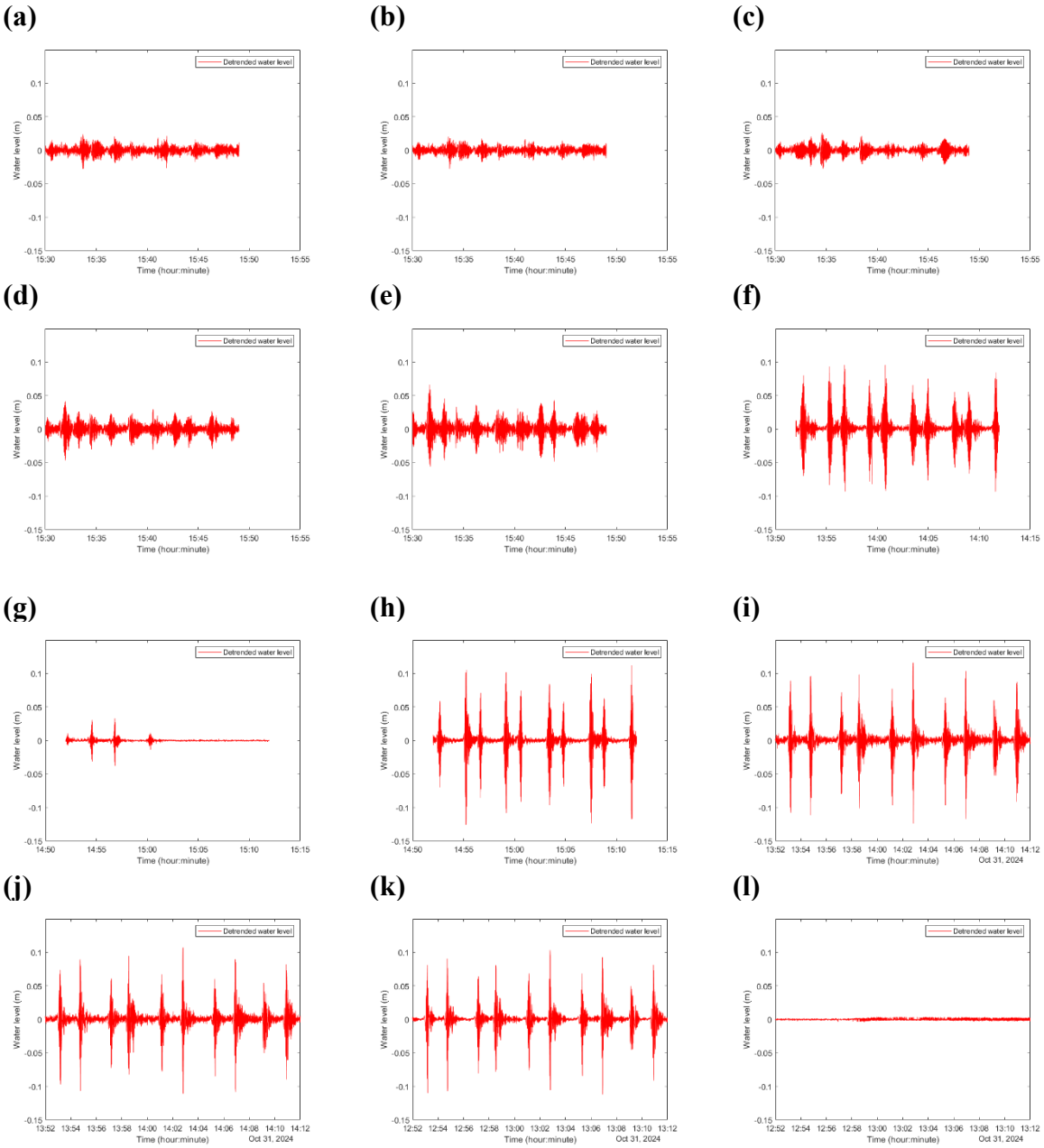

Figure A2. Water level variations over time after tidal signal removal for the S1 profile (PT1–PT5, panels a–e), S2 profile (PT1–PT3, panels f–h), and S3 profile (PT1–PT4, panels i–l), for boat velocity of 10 knots.

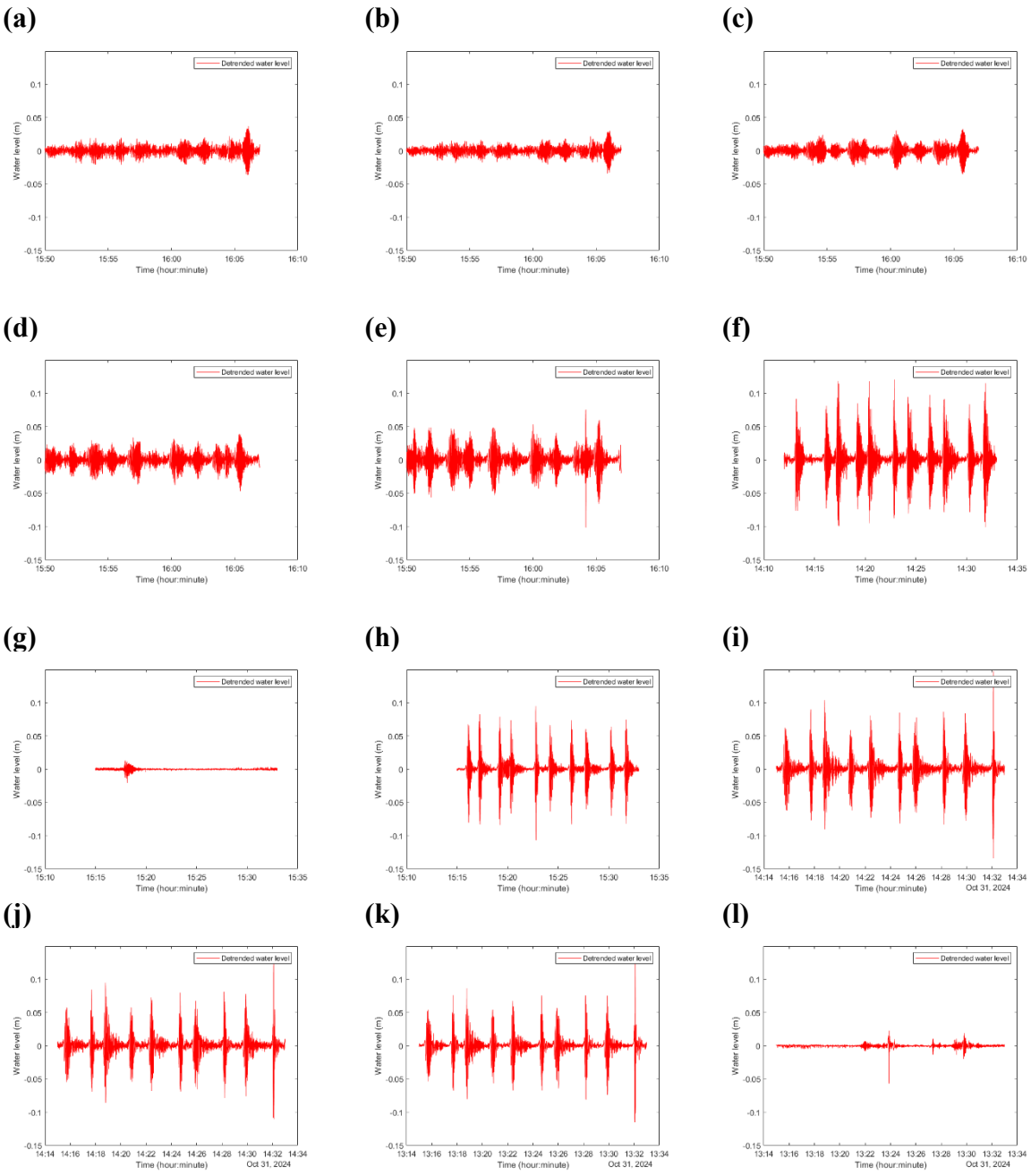

Figure A3. Water level variations over time after tidal signal removal for the S1 profile (PT1–PT5, panels a–e), S2 profile (PT1–PT3, panels f–h), and S3 profile (PT1–PT4, panels i–l), for boat velocity of 12 knots.

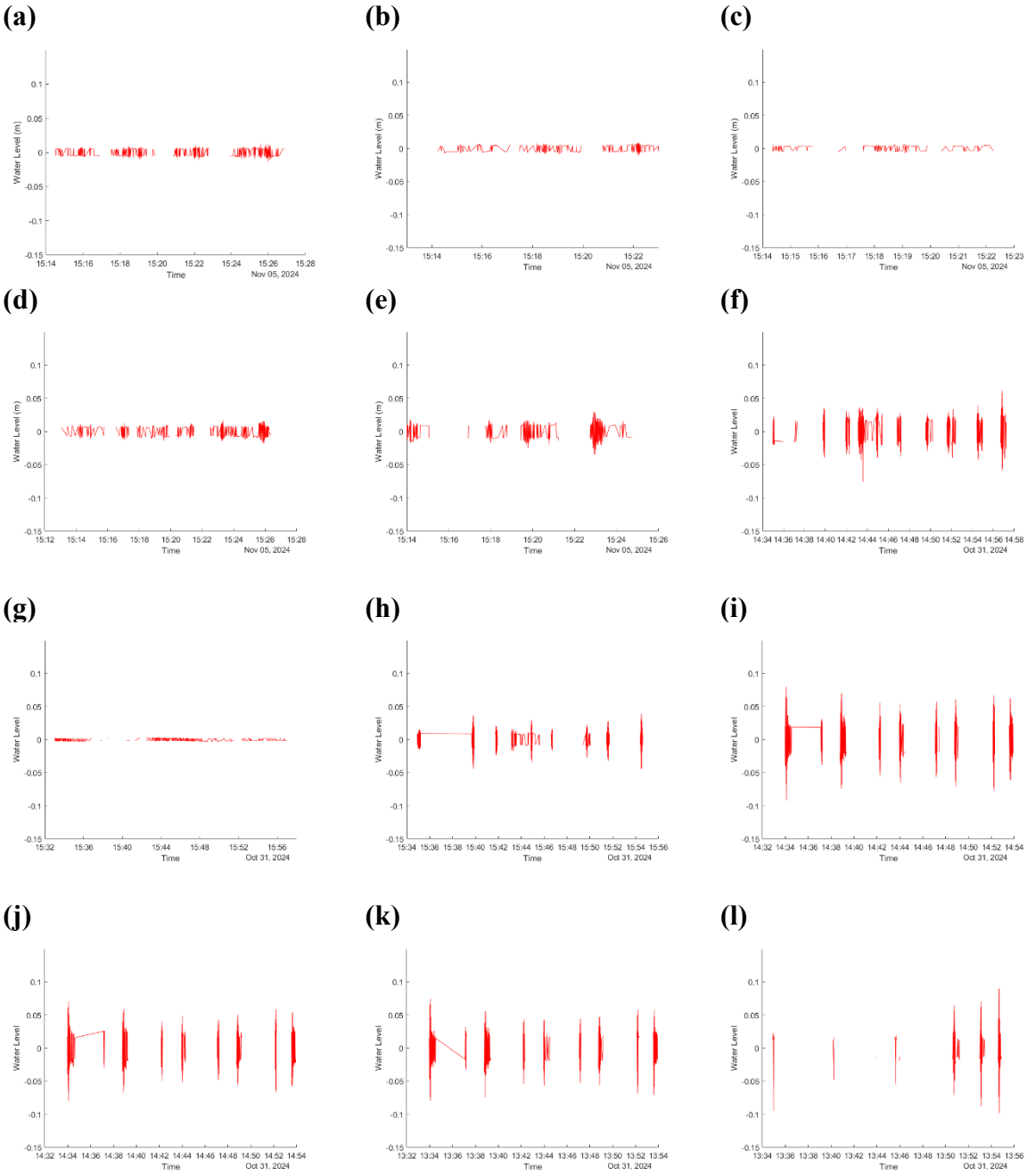

Figure A4. Water level variations over time after applying filter for the S1 profile (PT1–PT5, panels a–e), S2 profile (PT1–PT3, panels f–h), and S3 profile (PT1–PT4, panels i–l), for boat velocity of 8 knots.

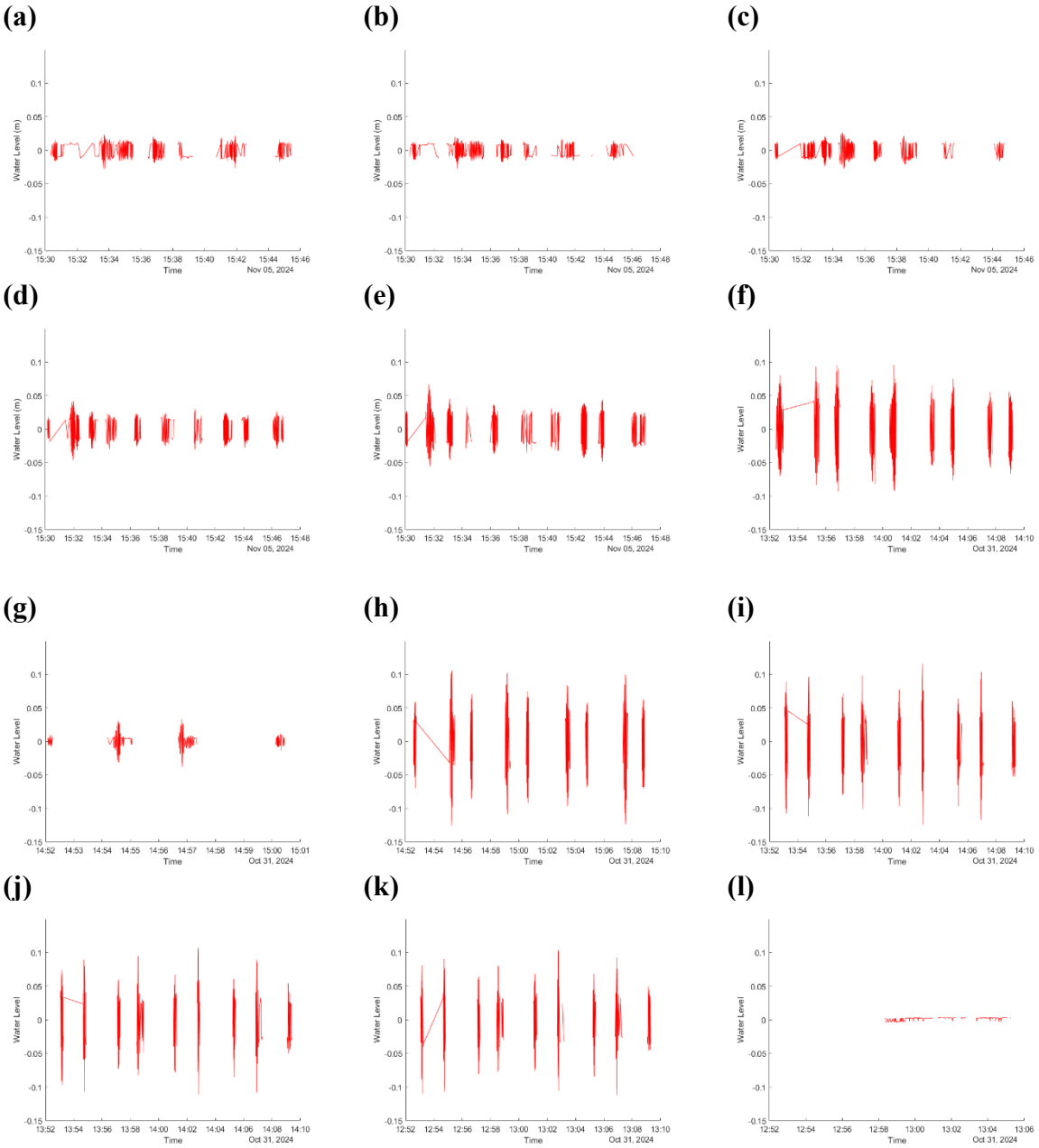

Figure A5. Water level variations over time after applying filter for the S1 profile (PT1–PT5, panels a–e), S2 profile (PT1–PT3, panels f–h), and S3 profile (PT1–PT4, panels i–l), for boat velocity of 10 knots.

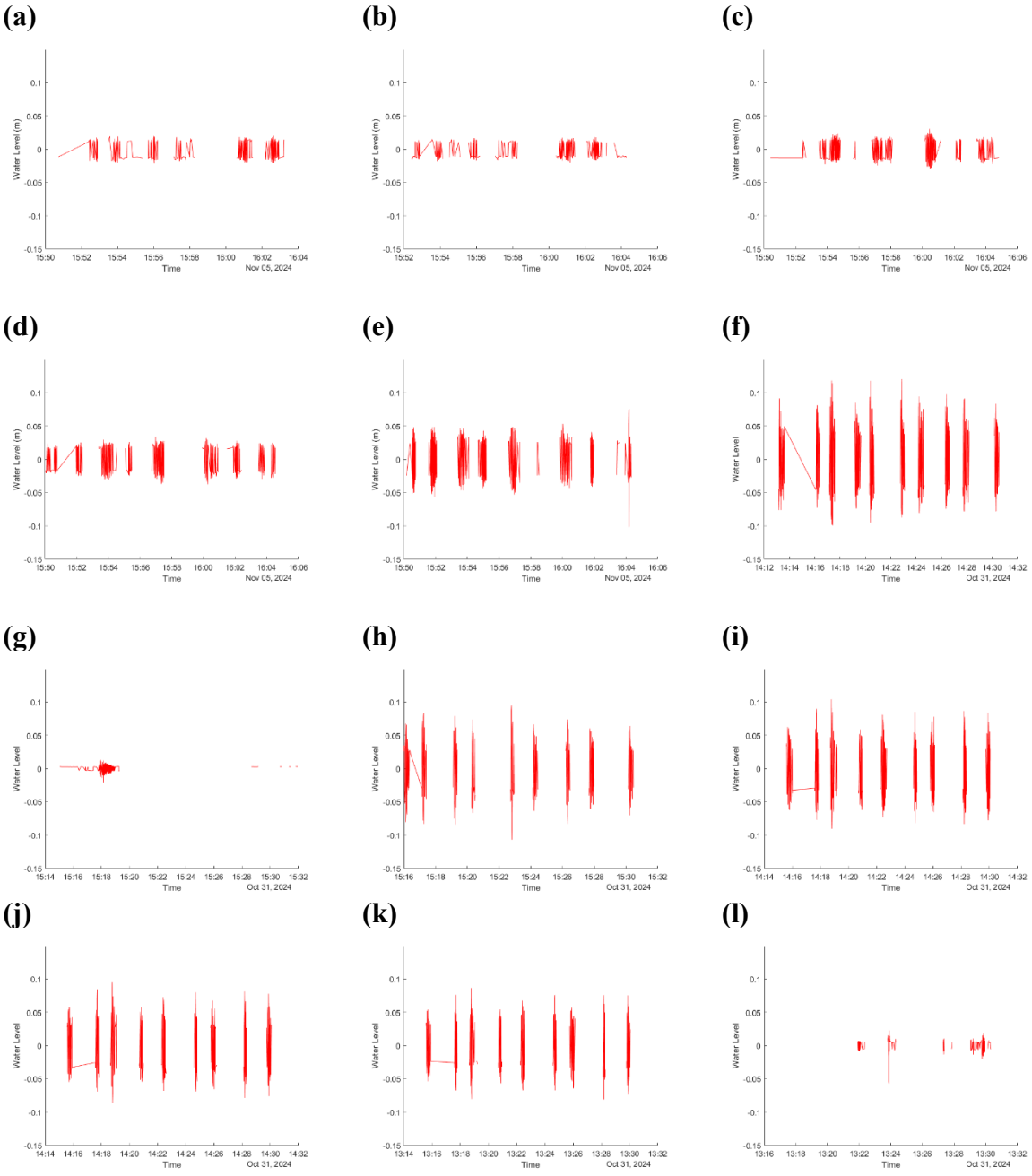

Figure A6. Water level variations over time after applying filter for the S1 profile (PT1–PT5, panels a–e), S2 profile (PT1–PT3, panels f–h), and S3 profile (PT1–PT4, panels i–l), for boat velocity of 12 knots.